Dalton Transactions

Effects of De-Fluorination on Hydrophobicity and on CO2 and CH4 Adsorption Under High Humidity in MeMOFs, Methylated Analogues of FMOFs

Journal:	*Dalton Transactions*
Manuscript ID	DT-ART-01-2025-000242.R1
Article Type:	Paper
Date Submitted by the Author:	08-Mar-2025
Complete List of Authors:	Yasmeen, Rashida; University of North Texas, Chemistry Islam, Sheikh; University of North Texas, Chemistry Ayeni, Olajumoke Mary; University of North Texas, Chemistry Moghadam, Peyman; UCL, Chemical Engineering and Biotechnology Du, Jincheng; University of North Texas, Material Science and Engineering Omary, Mohammad; University of North Texas, Chemistry

Effects of De-Fluorination on Hydrophobicity and on CO_2 and CH_4 Adsorption Under High Humidity in MeMOFs, Methylated Analogues of FMOFs

Rashida Yasmeen,[1] Sheikh M. S. Islam,[2] Olajumoke M. Ayeni,[2] Peyman Z. Moghadam,[3] Jincheng Du,[1,*] and Mohammad A. Omary[2,*]

[1]*Department of Materials Science & Engineering, University of North Texas, 1155 Union Circle, Denton, Texas-76203, United States*

[2]*Department of Chemistry, University of North Texas, 1155 Union Circle, Denton, Texas-76203, United States*

[3]*Department of Chemical Engineering, University College London, London WC1E 7JE, United Kingdom*

*Corresponding Authors. Email: Omary@unt.edu (M. A. O.); Jincheng.Du@unt.edu (J. D.)

ABSTRACT

Herein we report carbon dioxide (CO_2) and methane (CH_4) adsorption behavior in MeMOFs, methylated analogues of FMOFs with CF_3 groups altered to CH_3, utilizing Grand Canonical Monte Carlo (GCMC) simulations at 288, 298, and 308 K and P ≤ 40 bar and density-functional theory (DFT) computations of adsorption energies. Isosteric heat of adsorption (Q_{st}), Henry's constants (K_H) and interaction energies were used to analyze the adsorbate-adsorbent interaction strengths and gas uptakes of guest molecules. Q_{st} of CO_2 was found to be 1.29-1.73x higher in MeMOF-1 than in FMOF-1, vs 1.30-1.47x for CH_4, hence demonstrate higher guest affinity to MeMOF-1 than the same FMOF-1 polymorph. Simulated isotherms were further fitted with Langmuir, Langmuir-Freundlich and Tóth models to calculate the isosteric heat of adsorption at infinite dilution (Q_{st0}), using the Clausius-Clapeyron equation. The data were then compared with those obtained from force-field based Monte Carlo (MC) simulations to determine the consistency. The Tóth model presented excellent characterization of CO_2 and CH_4 adsorption, implying both FMOF-1 and MeMOF-1 materials have inhomogeneous surfaces. The order of the Q_{st0} values obtained using the Clausius-Clapeyron equation were persistent with the order of the Q_{st0} values obtained from MC and confirmed the higher uptake of CO_2 and CH_4 in MeMOF-1 predicted by GCMC. The presence of H_2O vapor, up to 80% relative humidity, did not affect the CO_2 and CH_4 adsorption in MeMOF-1 structures, as found in the analogous FMOF-1 parent structure. The larger pore size and surface area upon substituting CF_3 with CH_3 groups allows for significantly greater CO_2 and CH_4 uptake in MeMOFs vs FMOFs with no water uptake even at high humidity. The findings were applied for MeMOF analogues of multiple FMOF-1 polymorphs known to date and, thus, are expected to withhold for MeMOF analogues of other FMOF and MOFF structures reported by the Omary and Miljanić teams, respectively. Experimental data have

validated the superhydrophobic nature of the MeMOF-1 composition via a polymorphic form with a different topology, FMOF-2, attaining ~100° increase in water-drop contact angles, from ~74° for a control plastic substrate to ~172° upon dry-coating it with MeMOF-2. Experimentally synthesized MeMOF-2 possesses the same {Ag(3,5-$(CH_3)_2$-1,2,4-triazolate)} empirical formula of simulated MeMOF-1 structures, albeit with a different crystal structure and lower porosity.

1. INTRODUCTION

Global warming and climate change represent adverse impacts of CO_2, CH_4, and other greenhouse gas emissions.[1] CO_2 concentration has been noticeably increasing over time in the atmosphere mostly because of the combustion of fossil fuels.[2–5] Natural gas, which is predominantly composed of CH_4, has been argued to be a promising alternative to other fossil fuels (e.g., gasoline and coal) on the premise that its combustion produces ~50% less CO_2, albeit that ignores other environmental impacts of the hydraulic fracturing (fracking) process in expending and contamination of water resources. Nevertheless, the concomitant presence of CO_2 and N_2 in natural gas with the more desired CH_4 to decrease the energy production efficiency also adds to the challenges for using that technology.[6,7] Consequently, CO_2 capture and separation from CH_4 represent significant scientific and technological challenges with both environmental and economic significance.[8] Amine scrubbing,[9,10] membrane separation,[11,12] and solid adsorbent separation[13–15] are the three most widely-used methods for CO_2 removal. Among the traditional porous materials such as silica, activated carbons, and zeolites considered for selective carbon capture, adsorption processes using metal-organic frameworks (MOFs) has been garnering significant attention, in part due to the unique geometrical structures and tunable chemical properties of MOFs.[16–19] In order to enhance the CO_2 adsorption of MOFs, several methods have

been considered, such as creating narrow pores by structural interpenetration,[20,21] pore chemistry adjustment through cation exchange,[22–24] introducing "open" (coordinatively-unsaturated) metal sites,[25,26] and pore surface modification by ligand functionalization.[27–32] According to Li et al., the ligand functionalization is a promising approach to tune the adsorbate-adsorbent interaction,[23] which could enhance CO_2 adsorption in MOFs without significantly altering the overall structure of the parent MOF. However, pore structure, porosity and pore surface functionality could be greatly influenced due to the functionalization and should be considered when designing MOF functionalization. Another important consideration upon investigating MOF-based solutions for enhanced CO_2 and CH_4 adsorption is to investigate the hydrophobicity and the selective adsorption of CO_2 and CH_4 over water of the structures because the presence of water in humid or aqueous environments can adversely affect the CO_2 and CH_4 uptake.[33–36]

Fluorous metal-organic frameworks, such as the most heavily-investigated FMOF-1 composition = $Ag_2[Ag_4Tz_6]$, where Tz = 3,5-$(CF_3)_2$-1,2,4-triazolate, is a superhydrophobic MOF whose CO_2 uptake is not affected by the presence of water vapor at all.[37] In this paper, the ligand functionalization effect of -CH_3 upon CO_2 and CH_4 adsorption in MeMOF analogues of FMOF structures have been investigated using grand canonical Monte Carlo (GCMC) simulations. FMOF-1 was considered as the parent structure. To the best of our knowledge, CO_2 adsorption in FMOF-1 at 298 K was studied previously,[37] but neither CH_4 adsorption nor the effect of functionalization have been investigated before. As such, the aims of this study are two-fold: (1) to study the effect of functionalization by -CH_3 instead of -CF_3 groups on the CO_2 and CH_4 adsorption in the resultant hypothetical MeMOF-1 structures at three different temperatures (288, 298, and 308 K) up to 40 bar; and (2) to examine the hydrophobicity and selectivity of CO_2 and CH_4 over water in the resultant MeMOFs vs their parent FMOF counterparts. We have simulated

the CO_2 and CH_4 adsorption in both the parent and Me-functionalized FMOFs and investigated the Henry's constant (K_H) and isosteric heat of adsorption at infinite dilution (Q_{st0}) in order to understand the adsorbate-adsorbent interactions. These energy parameters acquired during the simulation were compared with the K_H values obtained by using the Tóth isotherm model and Q_{st0} values using Clausius-Clapeyron equation. By comparing the results, we summarized that the -CH_3 for -CF_3 substitution can greatly improve the CO_2 and CH_4 adsorption capacity in MeMOF-1, much more so than the merely subtle compromise in water rejection, hence resulting in not only similar but indeed greater CO_2/H_2O and CH_4/H_2O selectivity in MeMOFs vs FMOFs. The selective adsorption of CO_2 and CH_4 over water and the hydrophobicity of the structures were examined under high relative humidity conditions (RH = 80%). Overall, the computational findings in this work may pave the way for finding new experimental compositions that could be promising alternatives of fluorinated hydrophobic materials. This predictive work, therefore, represents the first step towards the development of a new chemical composition for fluorine-free adsorbents, coatings, or additives that may prove promising for this national/international endeavor to identify alternatives to Teflon, FMOF, ZIF, per- and poly-fluoroalkyl substances (PFAS), and other hydrophobic substances without compromise (indeed with potential improvement) of their pertinent desired properties and uses.

The goal of this work is to investigate the impact of de-fluorination of fluorinated metal-organic frameworks, by replacing F atoms with H atoms (e.g., $CF_3 \rightarrow CH_3$) in some known structures, on the water-rejection ability of the resulting frameworks during their CO_2 and CH_4 adsorption. Though the focus herein is upon some polymorphic forms of FMOF-1 among those known to date to attain methylated counterparts (MeMOFs), the strategy is expected to be applicable for other FMOF and MOF structures reported by the Omary[38,39] and Miljanić[40–44]

research teams, respectively. This work represents a first predictive step toward the development of alternatives of other classes of hydrophobic and/or omniphobic materials (ZIFs, COFs, FMOFs, MOFFs, PFAS, etc.) being investigated for such attributes.

2. METHODOLOGIES

2.1 Adsorbent Model

Yang et al. first synthesized FMOF-1 that consists of a perfluorinated structure.[45] FMOF-1c is the first adsorbent in this study which was acquired at 290 K and 61 bar under a carbon dioxide stream; CO_2 guest molecules were manually removed.[37] FMOF-1c (Figure 1a) has a tetragonal crystal structure with the space group $I\overline{4}\,2\,d$ and the lattice parameters are a = b = 14.0733 Å, c = 37.675 Å, $\alpha = \beta = \gamma = 90^0$. Considering FMOF-1c as the primary structure, MeMOF-1c was constructed by replacing the $-CF_3$ groups by $-CH_3$ while retaining the parent FMOF-1c 3D structure otherwise. After the replacement, the preliminary MeMOF-1c structure was optimized by using the Forcite module of Material Studio[46] shown in Figures S1-S2 (Supporting Information). Universal Force Field[47] describing the bonded and non-bonded interactions between the framework atoms was considered during the structure optimization. The final MeMOF-1c (Figure 1b) structure was obtained after finishing the two-step optimization process. We followed the same procedures for the optimization of MeMOF-1a and MeMOF-1b (Figure S3-S4), which represent analogous modification of FMOF-1a and FMOF-1b structures that correspond to the structures of FMOF-1 obtained under vacuum at 100 K and under a nitrogen stream at 90 K, respectively (N_2 molecules were manually removed from the FMOF-1b structure). Material Studio has the efficiency to generate feasible crystal structures and many researchers have been using this software to characterize MOF structures prior to their synthesis.[48–50] MeMOF-1c

has tetragonal crystal structure with the space group $I\overline{4}2d$ and the lattice parameters are a = b = 13.1532 Å, c = 37.2022 Å, $\alpha = \beta = \gamma = 90^0$. Both the FMOF-1c and MeMOF-1c possess two types of pores- smaller and larger. Smaller pores are marked by a red circle, whereas larger pores are denoted by a brown circle (Fig 1). Geometrical properties of the structures are shown in Table 1 and Table S2. The energy of the initial structure and the optimized MeMOF-1c are compared in Table S1.

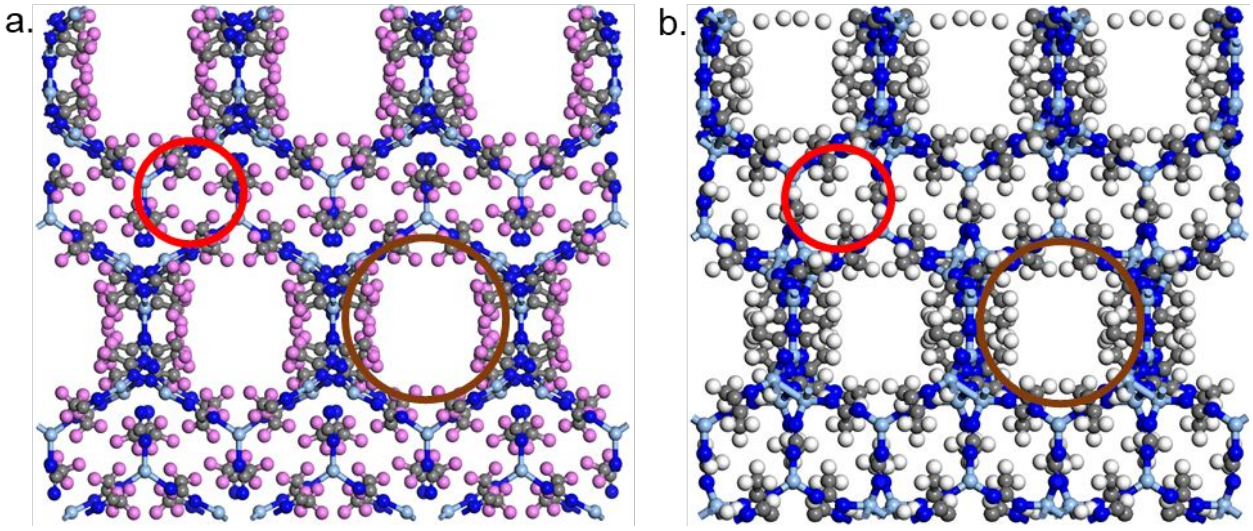

Figure 1. Crystal structures of (a) FMOF-1c and (b) MeMOF-1c. Color code (Ag: cyan, F: pink, N: blue, C: gray, and H: white).

2.2 Interaction Potential

To study the CO_2 and CH_4 adsorption in the pertinent MOFs herein, we account for theoretical models of the adsorbates and adsorbent and a force field that illustrates the adsorbate-adsorbent energetic interactions.[51] A combination of short-range Lennard-Jones (LJ) and long-range Coulomb potential was used to describe the non-bonded interactions, shown in Equation (1).

$$V_{ij} = 4\varepsilon_{ij}\left[\left(\frac{\sigma_{ij}}{r_{ij}}\right)^{12} - \left(\frac{\sigma_{ij}}{r_{ij}}\right)^{6}\right] + \frac{q_i q_j}{4\pi\epsilon_0 r_{ij}} \quad (1)$$

-- where the interacting atoms are indicated by i and j, r_{ij} is their interatomic distance, q_i and q_j are the partial atomic charges of i and j, respectively, ε_{ij} and σ_{ij} are the LJ potential parameters describing the well depth and repulsion distance between i and j, and ϵ_0 is the dielectric constant. The LJ parameters for the framework atoms were taken from the Universal Force Field (UFF).[47,52] The Lorentz-Berthelot mixing rules[53] were used to calculate the ε and σ parameters between different atom types. A cutoff length of 12.8 Å was considered for all LJ interactions and the tail corrections were ignored. Partial atomic charges are responsible for electrostatic interactions. The long-range electrostatic interactions were calculated by using the Ewald summation method.[54] The partial charges of -CF_3 groups in FMOF structures were taken from the work of Dalvi et al.,[55] whereas the Moghadam et al. work[37] provided the partial charges for the remaining FMOF atoms. In the functionalized structures (MeMOF-1a, MeMOF-1b, and MeMOF-1c), the partial charges of -CH_3 groups were calculated by using the connectivity-based atom contribution method (CBAC) described by Xu and Zhong.[56] CO_2 was modeled as a linear three-site rigid model with the C-O bond distance of 1.16 Å according to the TraPPE force field.[57] CH_4 was considered as a spherical single site model. LJ parameters and the partial charges of the framework atoms and adsorbates are represented in Table S3-S5. The Lennard-Jones parameters of CH_4 guest molecules were taken from TraPPE model[58] while water was described according to the TIP4P model.[59] The simulation box consisted of a supercell (2 × 2 × 1 unit cell) with periodic boundary conditions in all three directions for both structures. We modeled the MOFs as rigid; i.e., all framework atoms were kept fixed during the GCMC simulation. To explore the effect of framework flexibility on the adsorption properties, we performed simulations on three different MeMOF-1 crystal structures.

2.3 Simulation Details

Grand canonical Monte Carlo (GCMC)[53] simulations were performed by using the RASPA2 code[60] to study CO_2 and CH_4 adsorption isotherms. For each GCMC run, the number of gas molecules in the adsorbed phase was allowed to fluctuate while the chemical potential (μ), volume (V), and temperature (T) were kept constant. The isotherms were obtained by changing the pressure (P) and calculating the average number of adsorbed molecules (n) as an output of the simulations. Each MC simulation considered random insertion, deletion, rotation, and translation with equal probabilities. Fugacities and bulk densities of CO_2 and CH_4 were calculated according to the Peng-Robinson[61] equation of states. Excess adsorption isotherms were simulated by considering void fraction of both the structures (details can be found in the Supporting Information). At each pressure point, 1.0×10^5 cycles were used for equilibration and further 1.0×10^5 cycles for the adsorption properties determination of both CO_2 and CH_4. For pure and mixture water simulations, we have taken 5.0×10^5 cycles for equilibration followed by another 5.0×10^5 cycles for production runs.

Isosteric heat of adsorption at infinite dilution and the change of heat of adsorption with pressure were calculated using Equations (2) and (3) respectively:

$$Q_{St0} = -\Delta H = \langle U_{hg} \rangle - \langle U_h \rangle - \langle U_g \rangle - RT \quad (2)$$

$$\Delta H = \frac{\langle U \times N \rangle_\mu - \langle U \rangle_\mu \langle N \rangle_\mu}{\langle N^2 \rangle_\mu - \langle N \rangle_\mu^2} - \langle U_g \rangle - RT \quad (3)$$

-- where $\langle U_{hg} \rangle$, $\langle U_h \rangle$ and $\langle U_g \rangle$ are the average energies of the single guest molecule inside the host, the average energy of the host, the average energy of a single guest molecule in the gas phase, and N is the number of adsorbates in the system respectively. Henry's constant (K_H) of CO_2 and CH_4 were determined using the Widom insertion method[62] with 100,000 configurational biased insertions. K_H values were also obtained from the slope of the isotherms generated by using the Tóth parameters in the low-pressure regime. By applying the parameters

a_T, b_T and m acquired from the Tóth fit, we created loading (n)- pressure (p) data at the low-pressure region where there is a linear relation between n and p. Energy minimizations for a single adsorbate molecule inside FMOF-1c and MeMOF-1c were employed to investigate the contributions of van der Waals and Coulombic interactions to the adsorption energy. Baker's minimization method[63,64] for 100 independent minimization attempts with the stopping criteria of RMS gradient of 1.0×10^{-6} were considered. The geometrical properties of MOFs such as density, void fraction, pore volume, and channel diameter were computed using Zeo++ software.[65] The RASPA2 simulation code[60] was used to run all GCMC simulations.

The selective adsorption of CO_2 and CH_4 over water in FMOF-1c was calculated by using the Henry's constant ratio (Equation 4) and from the GCMC simulations (Equation 5).

$$S_{Henry} = \frac{K_{H,adsorbate}}{K_{H,H_2O}} \quad (4)$$

-- where $K_{H,adsorbate}$ and K_{H,H_2O} are the Henry's constants of the adsorbate (CO_2 or CH_4) and water, respectively.

$$S_{GCMC} = \frac{(q_{CO_2}/p_{CO_2})}{(q_{H_2O}/p_{H_2O})} \quad (5)$$

-- where q_i is the uptake of component i in mol/kg and p_i is the partial pressure of component i in Pa.

To validate the forcefield used in this study, we have first simulated the CO_2 adsorption in FMOF-1c at 298 K and compared it with the previously-simulated data (Figures S5-S6).[37] Our simulated data give rise to intermediate uptake and Q_{st} magnitudes between previously-reported isotherms, and exhibit similar trends and adsorption profiles. The isosteric heat of adsorption data showed better agreement with experimental data at very low loading and started to deviate around 2.300 mol/kg.

Density Functional Theory (DFT) utilizing the B97D/CEP-31G functional/basis set combination has been used to calculate the interaction energies. For the self-consistent field (SCF) convergence, we set the convergence criteria to 10^{-N} meaning that the convergence was achieved when the root mean square (RMS) change in the density matrix was less than 10^{-8} and a maximum change in the density matrix was less than 10^{-6}. The calculations were performed using the Gaussian 16 code;[66] further computational details can be found in Section 3.5.

2.4 Experimental Details for Synthesis and Contact Angle Measurements

MeMOF-2 is formed by the coordination of the ligand 3,5-dimethyl-1,2,4-triazolate to silver(I) ions, creating a three-dimensional coordination polymer network. The pure MeMOF-2 sample herein was synthesized upon modification of the method published by Zhai et al. in 2009.[67] A mixture of 1:1 molar ratio of 3,5-Me_2(1,2,4-TzH) and $AgNO_3$ (97.1 mg: 169.9 mg) was dissolved in 10 mL of methanol. To this, 5 mL of NH_4OH was added to de-protonate the triazole. The resultant solution was refluxed at 55 °C for 72 hrs. The precipitate was filtered, washed with cold ethanol and allowed to dry in the air to obtain a pure sample. Contact angle measurements were performed for a dry-coated surface of a 1 cm × 1 cm polyethylene terephthalate (PET) plastic substrate after sanding it with a 3M pro-grade precision P220 abrasive, following a procedure described by Chen et al.[68]

3. RESULTS AND DISCUSSION

Table 1. Geometric properties of the MOF structures studied in this work.

Structure	Density (g/cm^3)	Surface Area (m^2/g)	Void Fraction	Pore Volume (cm^3/g)	Channel Diameter (Å)
FMOF-1a	1.76[a]	817[a]	0.40[a]	0.22[a]	6.20[a]
MeMOF-1a	1.26[a]	1338[a]	0.48[a]	0.39[a]	6.44[a]
FMOF-1b	1.61[a]	903[a]	0.44[a]	0.28[a]	6.80[a]
MeMOF-1b	1.27[a]	1304[a]	0.46[a]	0.36[a]	6.21[a]
	1.66[a]	826[a]	0.41[a]	0.25[a]	6.73[a]
FMOF-1c	–	782[b]	0.41[b]	–	6.30[b]
	1.76[c]	842[c]	0.40[c]	0.23[c]	–
MeMOF-1c	1.24[a]	1425[a]	0.53[a]	0.42[a]	6.67[a]

[a] This work; [b] Moghadam et al.;[37] [c] Babarao et al.[69]

3.1 Adsorption Isotherms

Pure CO_2 and CH_4 adsorption isotherms were simulated in FMOF-1c and MeMOF-1c at 288, 298, and 308 K under a pressure range up to 40 bar. All simulation results are reported as excess quantities unless otherwise specified. Figure 2 represents the CO_2 and CH_4 uptake in FMOF-1c and MeMOF-1c. The order of CO_2 or CH_4 uptake was found to be much higher for MeMOF-1c than in FMOF-1c with the gas uptake of $CO_2 > CH_4$ for both FMOF-1 and MeMOF-1 materials at all temperatures. The result shows the effect of temperature on CO_2 and CH_4 adsorption capacity in the structures. For both FMOF-1c and MeMOF-1c, CO_2 and CH_4 uptake decreases with the increase in temperature, as expected for most porous materials. The CO_2 adsorption trend is found to be different from that of CH_4. Thus, our GCMC simulations herein

suggest a gradual increase of CO_2 uptake up to 20 bar, then reaching a plateau. Compared to CO_2, CH_4 exhibits almost linear isotherms up to 10 bar and does not saturate at 10 bar (in case of MeMOF-1c), not even at 35 bar (in case of FMOF-1c), consistent with the excellent experimental compressibility reported for this material upon extrapolating the experimental uptake within 0-55 bar up to 300 bar using the Tóth equation.[70]

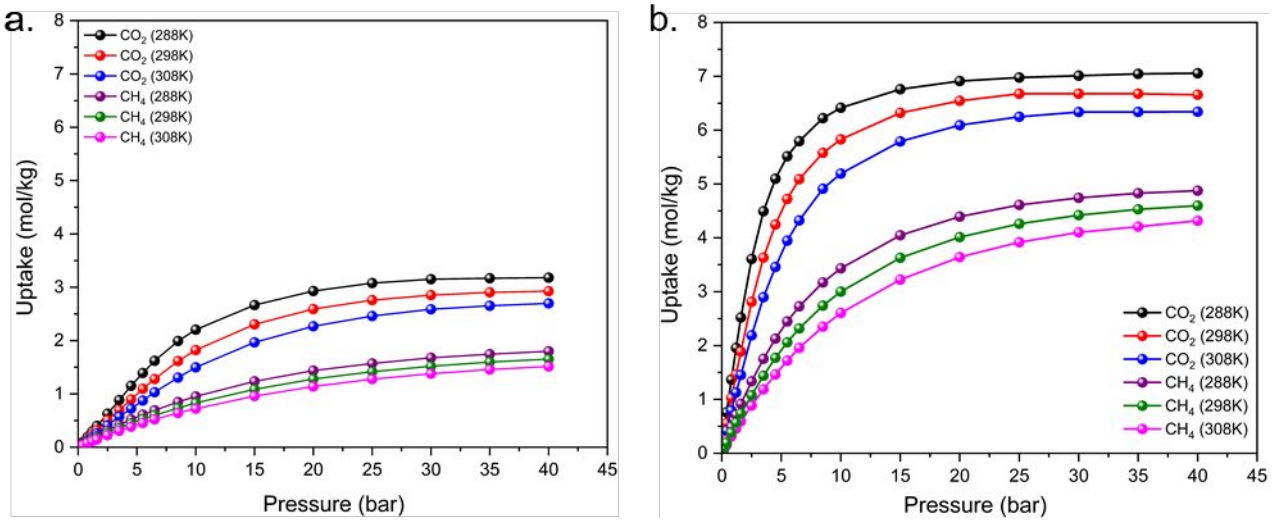

Figure 2. CO_2 and CH_4 adsorption isotherms of (a) FMOF-1c and (b) MeMOF-1c at 288, 298, and 308 K.

Figure 3a shows a comparison of CO_2 vs CH_4 adsorption isotherms of FMOF-1c and MeMOF-1c at 298 K. We notice a very sharp rise in CO_2 uptake for MeMOF-1c up to 10 bar, whereas FMOF-1c exhibits a continuous increase of CO_2 uptake up to 20 bar and then saturates gradually. However, a nearly linear increment of CH_4 uptake is suggested by these GCMC simulations in the low-pressure region for both structures. The very sharp rise of CO_2 uptake indicates a stronger CO_2–MeMOF-1c interaction than that of CO_2–FMOF-1c. The adsorption capacity of both CO_2 and CH_4 in MeMOF-1c is higher compared to FMOF-1c at 298 K. Similar trends are suggested at the two other temperatures simulated herein (288 and 308 K), as shown in Figures S7-S8.

When computing gas adsorption isotherms in MOFs, consideration of electrostatic interactions between the gas molecules and the framework atoms is crucial. To consider the electrostatic interactions, we must assign charges to the framework atoms. We have studied the influence of point charges on CO_2 adsorption for FMOF-1c at 298 K (Figure S5). CO_2 was considered for our study as it possesses a permanent quadrupole moment, whereas CH_4 is a zero-quadrupole-moment material. Consequently, CO_2 adsorption is sensitive to the charges of framework atoms, unlike CH_4 adsorption. In this study, FMOF-1c is considered the reference material, and MeMOF-1c is the methylated analogue of FMOF-1c. For the CO_2 adsorption isotherms in FMOF-1c, we used the charges from a previous simulation,[37] whereby -CF_3 charges were taken from Dalvi et al.[55] But for MeMOF-1c, we used charges based on the Connectivity-Based Atom Contribution (CBAC) method of Xu and Zhong[56] for the -CH_3 group; this method assigns charges to representative atoms of MOF building blocks with the same bonding environment. To make our analysis consistent, we used CBAC charges[56] for -CF_3 to simulate CO_2 adsorption isotherms in FMOF-1c and compared the results (Figure S5) with our former simulation. We observe a similar trend for CO_2 adsorption isotherm in FMOF-1c to both our previous simulation and experiment, indicating that the CBAC charge method has been validated for simulating the CO_2 adsorption isotherm in MeMOF-1c. We then studied the influence of point charges on CO_2 adsorption for MeMOF-1c at 298 K (Figure 3b) using two different charge methods, CBAC[56] and another common method for MOFs, the Extended Charge Equilibration (EQeq) method of Wilmer et al.[71] (by assigning point charges that minimize an energy function that describes properties such as electronegativities or ionization potentials specifically developed/optimized for MOFs). We observe a similar trend for those isotherms with little variation in CO_2 uptake, which suggests that both methods have been validated. Though different

charge methods might have different predictions for the amount of gas uptake, we did not observe any significant differences in CO_2 adsorption isotherms in the MeMOF-1c structure.

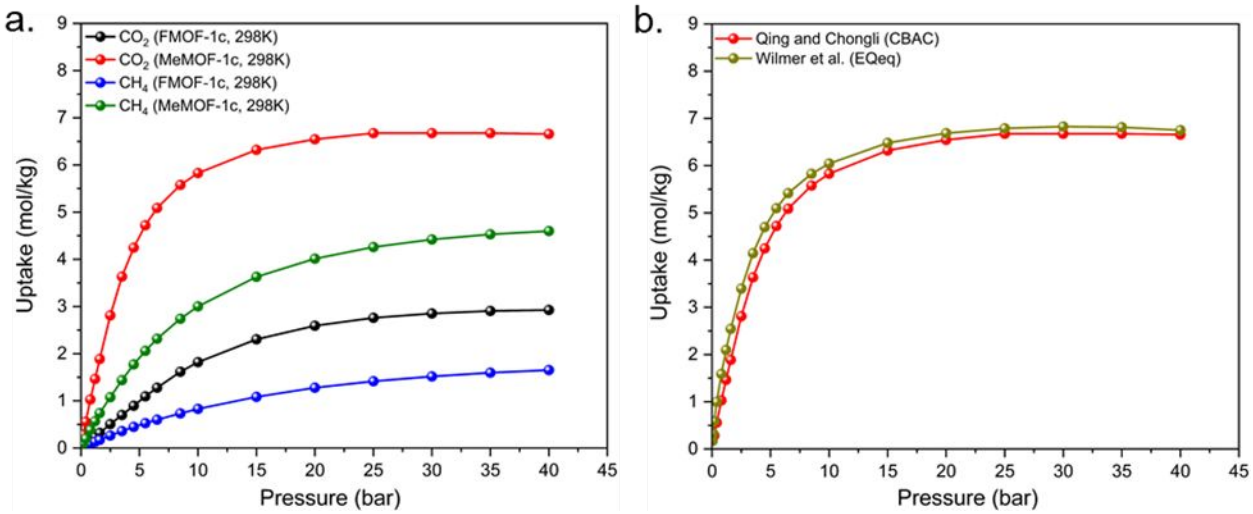

Figure 3. (a) Comparison of CO_2 and CH_4 adsorption isotherms of FMOF-1c and MeMOF-1c at 298 K. (b) CO_2 adsorption isotherms of MeMOF-1c using two different charge methods at 298 K.

In order to achieve a qualitative molecular level perspective of the guest molecules' adsorption behavior in each of the two MOFs, snapshots of CO_2 and CH_4 adsorption obtained from GCMC simulation in both the structures at 298 K and different pressures are displayed in Figures 4 and 5, respectively. According to Figure 4, at low pressure, CO_2 and CH_4 are preferentially adsorbed in the large cylindrical channel of FMOF-1c. As pressure increases, the guest molecules start to emerge near the small-cavity region. When the pressure is elevated further, both the cylindrical channel and the small cages would be gradually populated per these GCMC simulation. It is worth mentioning that the small cavities are not accessible in FMOF-1c at 278 K as per the simulation of Moghadam et al.[37] For MeMOF-1c shown in Figure 5, it can be observed that both the guest molecules would have occupancy near the small-cavity area at low pressure, in contrast with FMOF-1c. Gradually, the cylindrical channels and the small cages would be filled upon pressure increase.

We also simulated the CO_2 and CH_4 adsorption isotherms in MeMOF-1a and MeMOF-1b and compared them with the values obtained for MeMOF-1c at 298 K (Figure S9). As per Figure S9, greater CO_2 and CH_4 uptakes are obtained for MeMOF-1c (expanded structure under CO_2 atmosphere) compared to MeMOF-1a (rigid, guest-free, reference structure) or MeMOF-1b (expanded structure under N_2 atmosphere). While we compare adsorption capacities of MeMOF-1b and MeMOF-1c, we notice MeMOF-1c exhibits significantly higher CO_2 uptake than that of MeMOF-1b. We speculate this is due to the higher surface area of MeMOF-1c, 1425 m^2/g, vs 1308 m^2/g for MeMOF-1b.

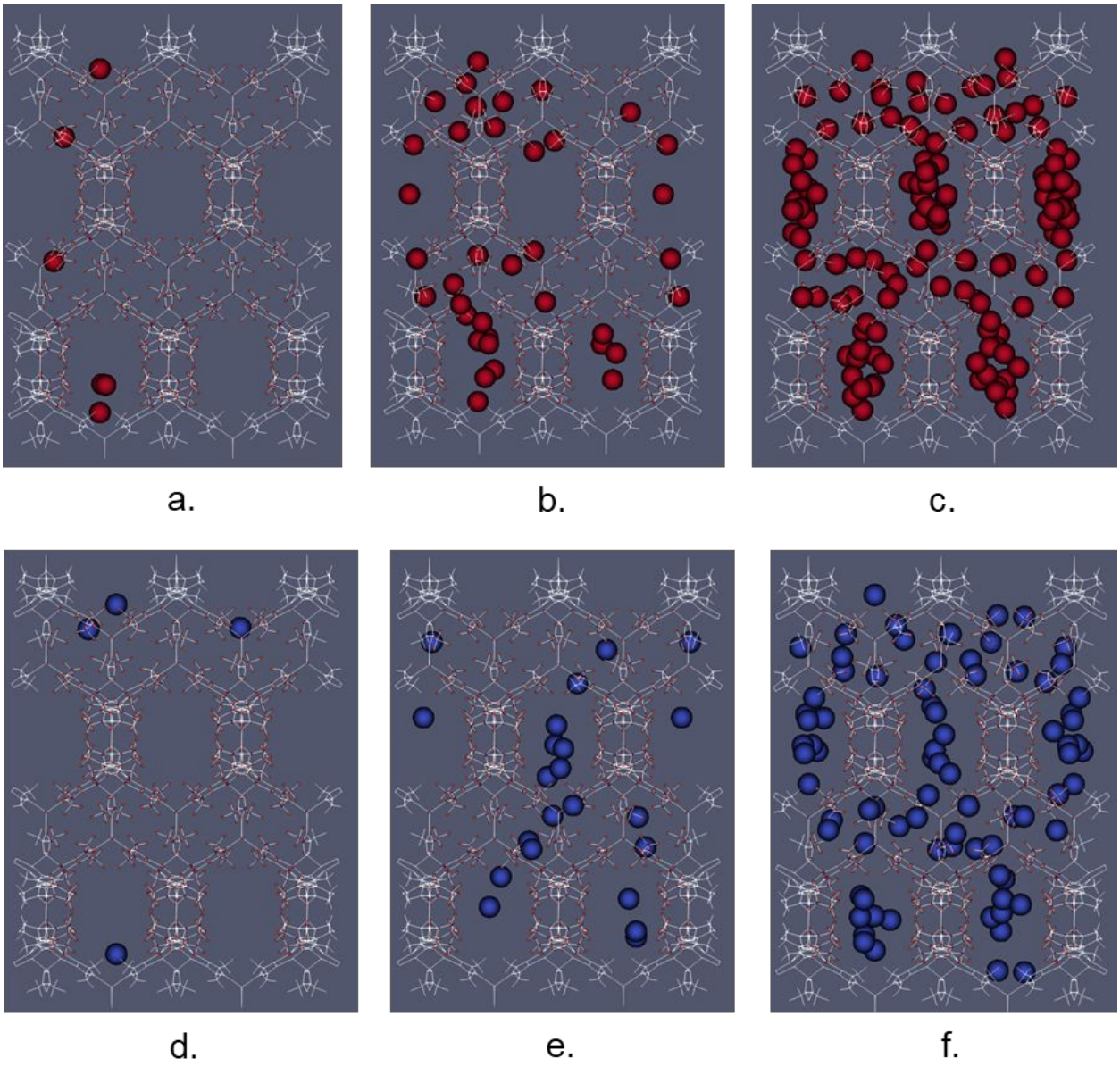

Figure 4. Snapshots at 1, 5, and 40 bar, respectively, of FMOF-1c for (a-c) CO_2 occupancy (red spheres) and (d-f) CH_4 occupancy (blue spheres).

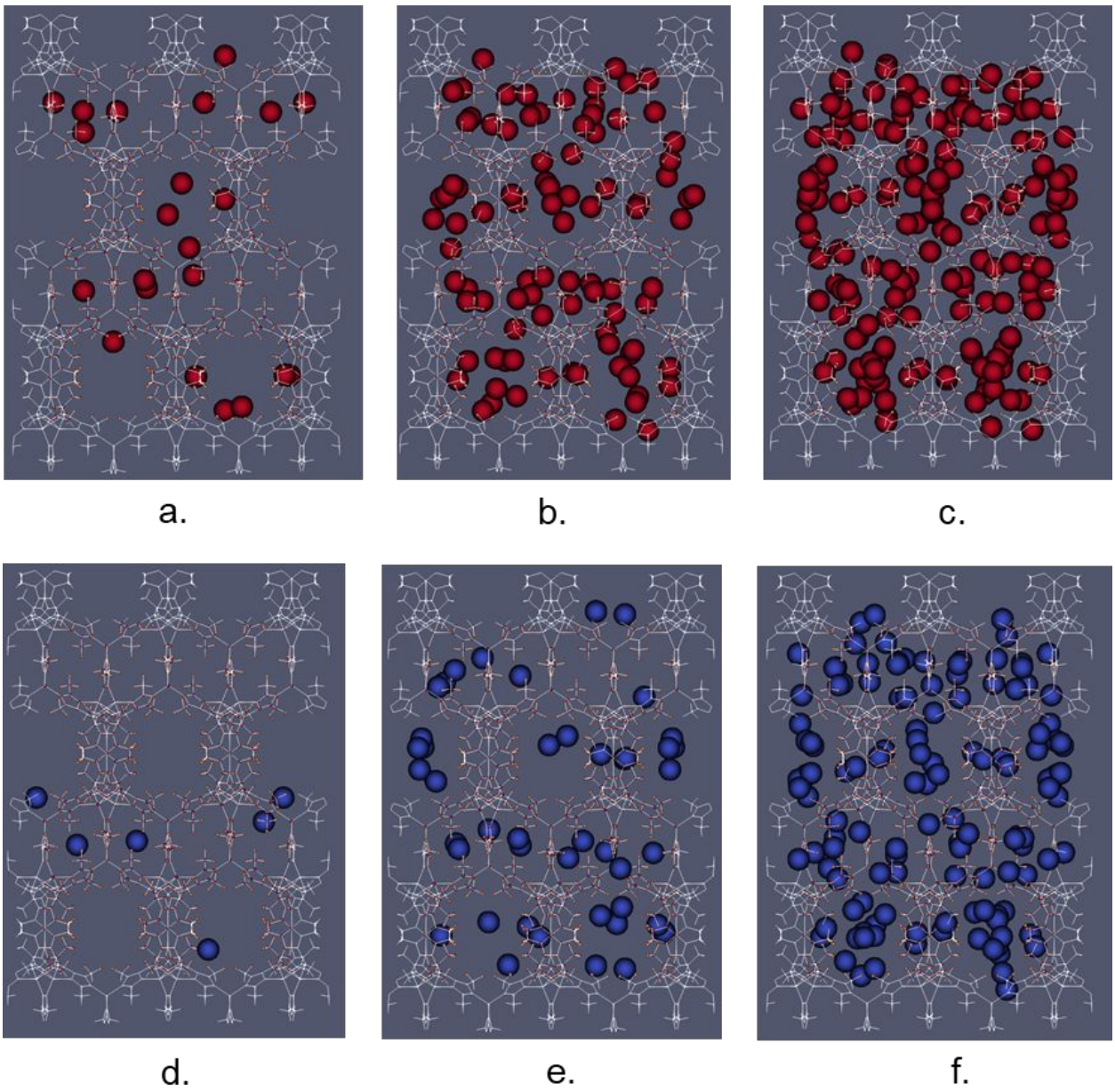

Figure 5. Snapshots at 1, 5, and 40 bar, respectively, of MeMOF-1c for (a-c) CO_2 occupancy (red spheres) and (d-f) CH_4 occupancy (blue spheres).

3.2 Isosteric Heats of Adsorption, Q_{st}

The isosteric heat of adsorption (Q_{st}) values at each isotherm pressure point were directly obtained during the adsorption isotherm simulations. The adsorption amount could be predicted by the magnitude of the isosteric heat of adsorption. The Q_{st} values for CO_2 and CH_4 adsorption of FMOF-1c and MeMOF-1c at 298 K are shown in Figure 6. In particular, Figure 6a compares

Q_{st} of CO_2 and CH_4 adsorption as a function of uptake, whereas Figure 6b presents Q_{st} as a function of pressure at 298 K. It is apparent that, for both structures, the Q_{st} value of CO_2 is larger than that of CH_4. So, the order of isosteric heat of adsorption is $CO_2 > CH_4$, consistent with the order of the adsorption capacity. The Q_{st} value of CO_2 for FMOF-1c rises evenly from ~14 to 23 kJ/mol (at 298 K), which slightly underestimates the reported Q_{st} values of CO_2 for FMOF-1c (Figure S6)., The Q_{st} values of CH_4 also exhibit an increasing trend from ~11 to 14 kJ/mol for FMOF-1c. This increasing behavior is probably due to the lateral interactions of the guest molecules with the rise in pressure (or the adsorbate concentration).[72–74] On the other hand, the Q_{st} value of CO_2 adsorption for MeMOF-1c first declines from 24 to 22 kJ/mol, up to around 2.5 mol/kg (Figure 6a) or 1.2 bar (Figure 6b). After that, it increases rapidly. This indicates that the CO_2–MeMOF-1c interactions dominate the adsorption at low loading levels, whereas the contribution of CO_2–CO_2 interactions escalates after preferential site occupation. The Q_{st} values of CH_4 adsorption remains almost unchanged over the entire pressure range due to adsorption sites saturation.[75,76] For MeMOF-1c, we observe a larger number of guest molecules (both CO_2 and CH_4) than that for FMOF-1c, ensuing a higher condensed phase at a particular pressure compared to FMOF-1c. Subsequently, the isosteric heats of adsorption for both CO_2 and CH_4 of MeMOF-1c is larger than that of FMOF-1c. Since Q_{st} values are lower than 40 kJ/mol, therefore the CO_2 and CH_4 adsorptions in the considered MOF structures is a physisorption process.[77] The Q_{st} values at the other two temperatures are depicted in Figures S10-S12.

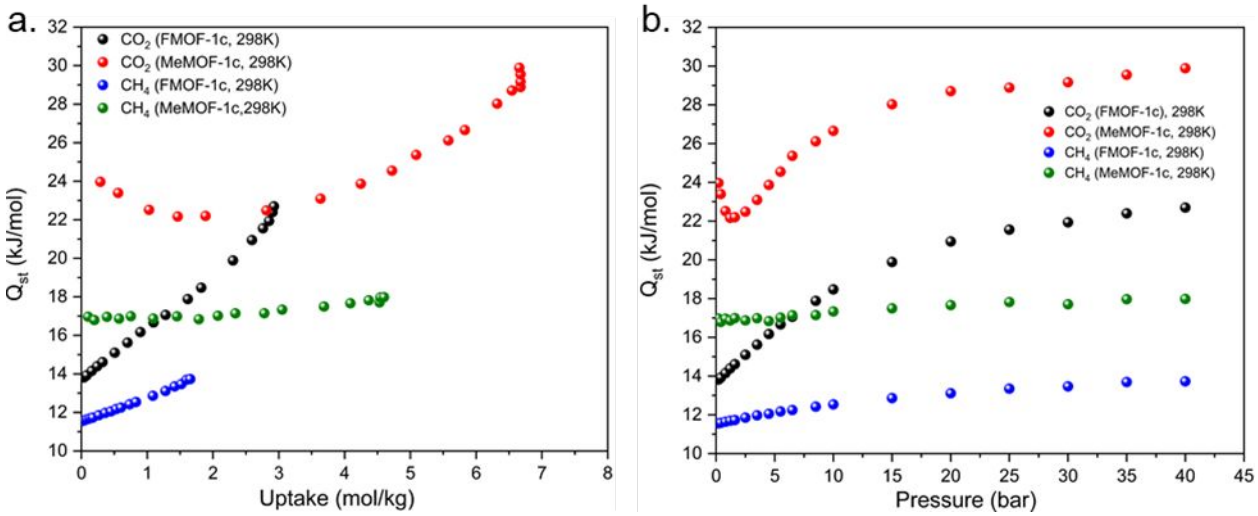

Figure 6. Simulated isosteric heats of adsorption, Q_{st}, for CO_2 and CH_4 of FMOF-1c and MeMOF-1c: (a) as a function of uptake and (b) as a function of pressure at 298 K.

We also studied the Q_{st} of CO_2 and CH_4 adsorption for MeMOF-1a and MeMOF-1b followed by comparing them with MeMOF-1c data at 298 K (Figure S14). Table 2 displays the Q_{st0} values of the CO_2 and CH_4 adsorbates at 298 K. For all the adsorbents, the Q_{st} values of CO_2 adsorption initially exhibit a decreasing trend up to 1.4 mol/kg (corresponding to 2 bar) and then an increasing trend is attained. The Q_{st} values of CH_4 adsorption remains almost unchanged throughout the entire loading/pressure range. According to Figure S14, MeMOF-1c exhibits the highest Q_{st0} values vs the other two adsorbents, both for CO_2 and CH_4. Generally, the smaller pores of porous materials usually display higher Q_{st} values, as smaller pores have shorter distances between the pore walls that result in stronger adsorbate-adsorbent interactions.[78,79] The highest Q_{st} values at low loading for MeMOF-1c is due to the strong adsorption of adsorbates (CO_2 and CH_4) in the small-cavity region (Figure 5). While we compare Q_{st} of MeMOF-1a and MeMOF-1b, we notice MeMOF-1b exhibits higher values vs those for MeMOF-1a. We speculate this to be due to the smaller small-pore diameter of MeMOF-1b (6.21 Å) than MeMOF-1a (6.44 Å), even though the large-channel diameters have the opposite trend.

Table 2. Q_{st0} values for CO_2 and CH_4 in methyl-functionalized MeMOFs, structural analogues of FMOF structures.

Adsorbent	Qst_0 (kJ/mol)	
	CO_2	CH_4
MeMOF-1a	20.20	14.16
MeMOF-1b	21.36	15.08
MeMOF-1c	24.51	17.02

Adsorbate-adsorbent interaction strength can also be characterized by studying the heat of adsorption at infinite dilution, Q_{st0}. A stronger interaction between the gas adsorbate molecule and the host MOF material is reflected by greater Q_{st0}.[80] Likewise, Henry's constant, K_H, can portray the adsorbate affinity to the adsorbent. The large K_H value represents greater affinity of the adsorbate. Both K_H and Q_{st0} were estimated from Widom insertion method, and the results are presented in Figures 7a and 7b, respectively.

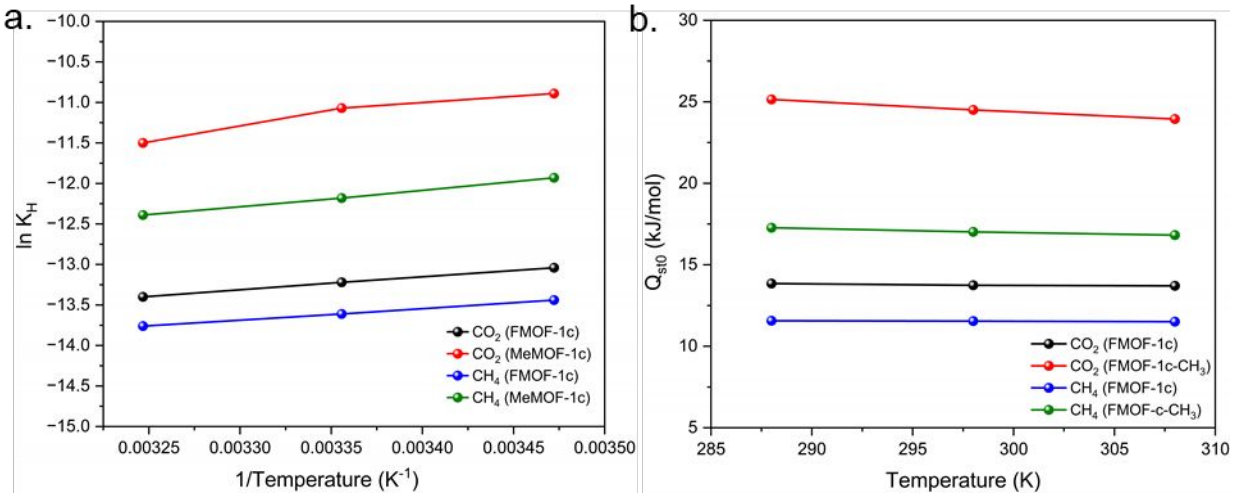

Figure 7. (a) Henry's constant, K_H, and (b) isosteric heat of adsorption at infinite dilution, Q_{st0}, for CO_2 and CH_4 at various temperatures in MeOF-1c and FMOF-1c structures, obtained from Widom insertion method.

The Henry's constant of CO_2 in the studied MOFs was found to be about one-and-a-half-fold larger than that of CH_4, whereas the ratio of CO_2/CH_4 isosteric heats of adsorption at infinite dilution was around 1.2-fold larger. According to this finding, the order of the affinity is $CO_2 > CH_4$, which could be due to the permanent quadrupole moment of the CO_2 molecule that generates an electrostatic force.[80] The K_H values for CO_2 adsorption in MeMOF-1c are found to be more sensitive to temperature changes in comparison with FMOF-1c slowly decreased with increased temperature. At 298 K, the K_H and Q_{st0} values for CO_2 adsorption in FMOF-1c are 1.81×10^{-6} mol/kg/Pa and 13.71 kJ/mol, respectively. The analogous values obtained for CO_2 adsorption in MeMOF-1c are 1.56×10^{-5} mol/kg/Pa and 24.51 kJ/mol, respectively. Likewise, our MC simulations (Widom insertion) predict larger K_H and Q_{st0} values for the CH_4 adsorption in MeMOF-1c than that in FMOF-1c. Hence, it can be summarized that CO_2 and CH_4 exhibit greater affinity and stronger interaction strength in MeMOF-1c than in FMOF-1c, which can be attributed to the Me group ligand functionalization.

Figure S15 displays the percentage increase of both CO_2 and CH_4 uptake and isosteric heat of adsorption at infinite dilution as a contribution of $-CH_3$ functionalization in MeMOF-1c. The $(N_{MeMOF\text{-}1c} - N_{FMOF\text{-}1c})/ N_{FMOF\text{-}1c}$ ratio was used to calculate the increased percentages of adsorption. Here, $N_{MeMOF\text{-}1c}$ and $N_{FMOF\text{-}1c}$ denote the amounts of adsorbates adsorbed in functionalized (MeMOF-1c) and parent (FMOF-1c) MOFs, respectively, at 1 bar and 298 K. For isosteric heat of adsorption at infinite dilution, the comparison was via the $(Q_{st0\text{-}MeMOF\text{-}1c} - Q_{st0\text{-}FMOF\text{-}1c})/ Q_{st0\text{-}FMOF\text{-}1c}$ ratio, where $Q_{st0\text{-}MeMOF\text{-}1c}$ and $Q_{st0\text{-}FMOF\text{-}1c}$ represent the isosteric heat for the methyl-functionalized MeMOF and the parent FMOF, respectively.

The larger uptake of CO_2 in MeMOF-1b compared to MeMOF-1a at the low-pressure region (Figure S9) could be described by K_H values for CO_2 in the 298 K structures (Figure S16).

Since K_H describes adsorbate-adsorbent interactions ignoring adsorbate-adsorbate interactions, the larger K_H for CO_2 in MeMOF-1b indicates larger CO_2–MeMOF-1b interaction compared to CO_2–MeMOF-1a interaction, resulting in higher uptake in MeMOF-1b up to around 5 bar, whereby adsorbate-adsorbent interactions play the dominant role for the CO_2 adsorption.

3.3 Interaction Energy Effects

The interaction energy contributions to the adsorption mechanism of CO_2 and CH_4 in FMOF-1c and MeMOF-1c at 298 K, as presented in Figures 8 and S17-S26, are consistent with the discussion in Section 3.2. The percentage portion of the guest-guest and host-guest energy contribution to the total energy values shows that the host-guest interaction energy decreases vs increased pressure up to 40 bar. In contrast, the guest-guest interaction energy rises during CO_2 and CH_4 adsorption for both structures, up to the 40 bar pressure range.

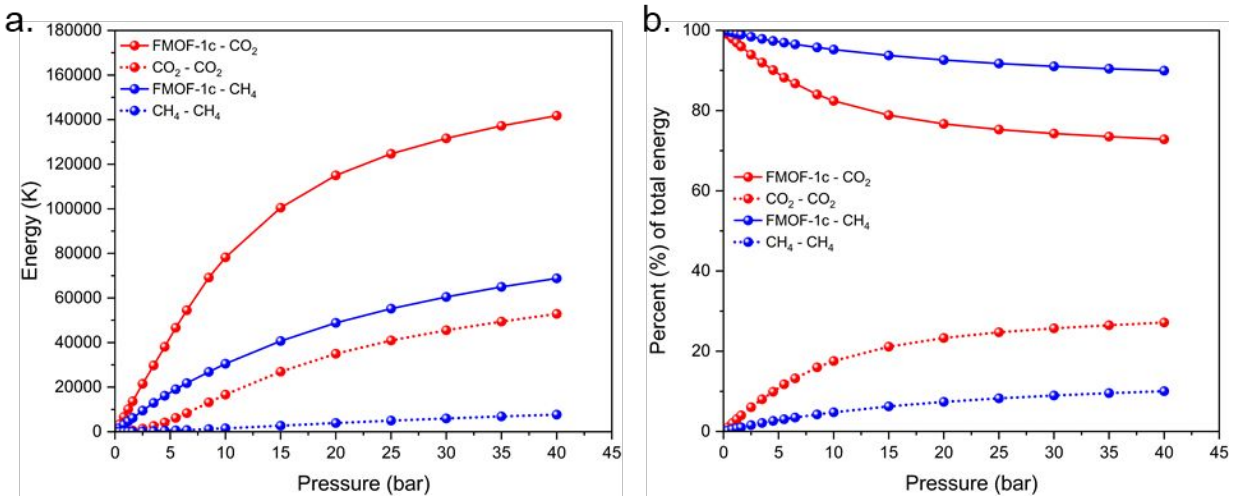

Figure 8. The breakdown of (a) total potential energy and (b) percentage of total potential energy into host-guest and guest-guest contribution for CO_2 and CH_4 adsorptions in FMOF-1c, obtained from GCMC simulations at 298 K.

Figure S27 exhibits the relative contribution of van der Waals (vdW) and Coulombic interactions of the total adsorption energy of CO_2 and CH_4 in FMOF-1c and MeMOF-1c. The CO_2 interaction is significantly stronger than the CH_4 interaction in analogous FMOF and MeMOF

structures. Additionally, MeMOF-1c displays stronger interactions compared to those in FMOF-1c for both CO_2 and CH_4 adsorptions. The CH_4 model used in our simulation's possess no charges. Therefore, no electrostatic interactions are present among the CH_4 molecules and MOF atoms. Consequently, the adsorption energy for CH_4 stems purely from the van der Waals interactions. For CO_2, on the other hand, the collective interaction consists of both vdW and Coulombic interactions -- with the Coulombic interaction contribution being relatively small vs vdW interaction (20% vs 80%, respectively). All these data establish that the functionalization/de-fluorination of FMOF-1c to MeMOF-1c (i.e., replacing -CF_3 by -CH_3 groups) leads to increased adsorption energy.

Figure 9 depicts the adsorbate positions in FMOFs after Baker's minimization.[63,64] The nearest distances between CO_2---F_CF_3 and CH_4---F_CF_3 are 3.88 and 4.45 Å, respectively, in FMOF-1c. On the other hand, the nearest distances between CO_2---H_CH_3 and CH_4---H_CH_3 are 3.18 and 3.82 Å, respectively, in MeMOF-1c after minimization. Apparently, CO_2 and CH_4 molecules are much closer to the H_CH_3 in MeMOF-1c compared to the F_CF_3 in FMOF-1c, with the values of 0.70 and 0.63 Å, respectively. It should be noted that the covalent radii of F and H are 0.71 and 0.37 Å, respectively.[81] Given that the differences between the Guest---H and Guest---F distances (0.70 and 0.63 Å) are higher than the difference between the covalent radii of F and H (0.34 Å), these results suggest genuinely stronger interactions of both adsorbates with MeMOF than with FMOF adsorbents.

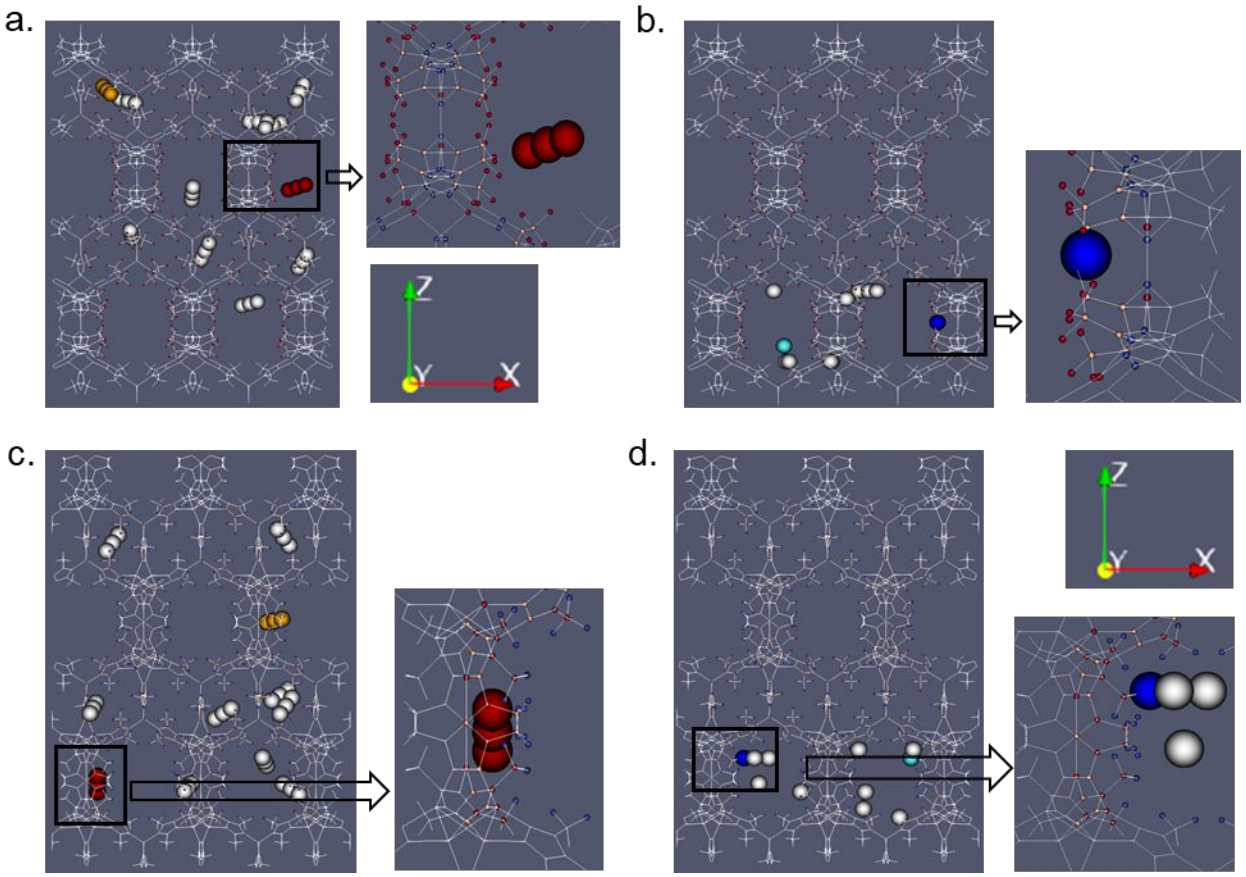

Figure 9. Adsorption sites of (a) CO_2 and (b) CH_4 in FMOF-1c; (c) CO_2 and (d) CH_4 in MeMOF-1c. Initial and final (after minimization) positions of CO_2 are represented by orange and dark-red spheres, respectively, while analogous symbols for CH_4 are shown as cyan and dark-blue spheres, respectively; gray spheres represent different positions of molecules during minimization with some points omitted for clarity purposes.

3.4 Isotherm Models

The adsorption isotherms obtained from the molecular simulations were fitted using three different models: Langmuir, Langmuir-Freundlich (L-F) and Tóth models. The goodness-of-fitting in each model with respect to the adsorption isotherms were assessed from the residual root mean square error and the chi-square test -- i.e., *RMSE* and χ^2, respectively. Details can be found in the Supporting Information. Figures S28-S30 depict the fitting curves of adsorbates for FMOF-1c at 288, 298, and 308 K. The fitting parameters and goodness-of-fitting parameters are presented in Tables S6 (Langmuir), S7 (Freundlich-Langmuir), and S8 (Tóth) for FMOF-1c.

As summarized in Table S8, the comparison of a_T parameter at all temperatures suggests a_T (CO_2) > a_T (CH_4), indicating CO_2 reaches saturation and exhibits higher maximum uptake vs CH_4. The order of magnitude of the pressure required by the gas to attain the stable point also entails CH_4 > CO_2, suggested by b_T, which is inversely proportional to the pressure needed for saturation. As a result, one notices a higher CO_2 adsorption vs CH_4 in the low-pressure region.

The smallest *RMSE* and χ^2 values for the Tóth model entails the best fitting for CO_2 and CH_4 isotherms in FMOF-1c vs the other models. For CO_2, the Langmuir model underestimates the uptake near 1.0×10^6 Pa to 3.0×10^6 Pa while it overpredicts at very low and high-pressure regions. All models show better fitting for CH_4 vs CO_2. From the Tóth model in FMOF-1c, we observe a deviation of the heterogeneity parameter from unity, suggesting that FMOF-1c acts as a heterogenous surface during the adsorption for both adsorbates. The same summary can be made while comparing the models for MeMOF-1c, as shown in Figures S49- S51 and from the fitting parameters given in Tables S9 (Langmuir), S10 (Langmuir-Freundlich) and S11 (Tóth).

The isosteric heats of adsorption at infinite dilution (Q_{st0}) were calculated using Clausius-Clapeyron equation[82] approach (Supporting Information) based on the pure component CO_2 and CH_4 adsorption isotherms at 288, 298, and 308 K obtained by GCMC simulation. Since the Tóth model showed the best characterization of CO_2 and CH_4 adsorption in MOFs, we have used the Tóth model parameters to generate pressure (p)/loading (n) pairs to estimate the Q_{st0} values. We have compared the isosteric heats of adsorption at infinite dilution (Q_{st0}) values obtained by the Clausius-Clapeyron equation to the values acquired by MC simulation (using Widom insertion method) at different temperatures **(**Table 3**)**. The results are comparable for CH_4, while for CO_2, the Q_{st0} values are higher for Clausius-Clapeyron method. It should be worth mentioning that our

calculated Q_{st0} value for CO_2 at 298 K in FMOF-1c (16.95 kJ/mol) using Clausius-Clapeyron equation is comparable to the reported value (16.49 kJ/mol)[69] found in literature.

Table 3. Q_{st0} (kJ/mol) for CO_2 and CH_4 adsorption of FMOF-1c and MeMOF-1c.

Guest	Adsorbent	Qst$_0$ (Clausius-Clapeyron)	Qst$_0$ (MC/288 K)	Qst$_0$ (MC/298 K)	Qst$_0$ (MC/308 K)
CO_2	FMOF-1c	16.95	13.85 ± 2.56	13.71 ± 2.49	13.69 ± 2.41
	MeMOF-1c	30.58	25.15 ± 2.67	24.51 ± 2.61	23.95 ± 2.50
CH_4	FMOF-1c	11.28	11.60 ± 2.56	11.54 ± 2.48	11.48 ± 2.40
	MeMOF-1c	18.24	17.28 ± 2.64	17.02 ± 2.57	16.82 ± 2.47

We also compared Henry's constants of CO_2 and CH_4 obtained from the Widom insertion method[62] using RASPA2 ($K_{H,\ RASPA}$) with the values ($K_{H,\ Tóth}$) calculated from the slope of the isotherms generated by using the Tóth parameters in the low-pressure regime. Figures S70-S73 depict the pressure range used for K_H calculations in MOFs and the results are summarized in Table S12, showing a satisfactory agreement between the two sets of values.

3.5 Interaction energies from DFT calculations

Density Functional Theory- (DFT-) based calculations have also been used to obtain the interaction energy (IE) of the adsorbates (CO_2 and CH_4) with -CF_3, in FMOF-1c and -CH_3, in MeMOF-1c (Table 4 and Figure 10a-d). The density functional B97D along with the CEP-31G basis set were used in this study using Gaussian16 code.[66] Only the triazole bearing the two -CF_3 or two -CH_3 substituents in the 3,5- positions was used in the molecular model for interaction with CO_2 or CH_4 (see Figure 10), in order to render such high-accuracy DFT computations that account

for dispersion (physisorption/van der Waals interactions) feasible. For the convergence of the optimized structures, we examined the "Maximum Force" and "RMS Force" values within the optimization output, to make sure they fall below the predefined thresholds values. In Gaussian 16, the default threshold values for "Maximum Force" and "RMS Force" during a geometry optimization are typically set to 0.000450 Hartree/Bohr and 0.000300 Hartree/Bohr, respectively. The lower values of "Maximum Force" and "RMS Force" than that of the threshold values ensured the convergence of the optimized structures, shown in Figure 10.

Table 4. DFT-based (B97D/CEP-31G) interaction energy of CO_2 and CH_4 in small molecular models for FMOF and MeMOF.

Adsorbate	Substituent	Interaction Energy (kJ/mol)
CO_2	$-CF_3$ (FMOF-1c)	-18.20
	$-CH_3$ (MeMOF-1c)	-22.46
CH_4	$-CF_3$ (FMOF-1c)	-6.00
	$-CH_3$ (MeMOF-1c)	-11.33

As per Table 4, the interaction energy of CO_2 is higher than that of CH_4 for both FMOF-1c and MeMOF-1c. It is also observed that, the $-CH_3$ functionalization affords stronger interaction with CO_2 and CH_4, compared to the parent $-CF_3$ functionalization. The results are very consistent with the Q_{st0} values, either obtained from MC simulation or via the Clausius-Clapeyron equation. The interaction energy between CO_2 and the $-CH_3$ groups is -22.46 kJ/mol, which is comparable to the interaction energy reported by the work of Gu et al.[83] The larger interaction energy of CO_2 compared to CH_4 can be, at least in part, ascribed to the quadrupole moment of CO_2.[84] We observe a smaller distance between O_CO_2 and H_CH_3 in comparison with O_CO_2 and F_CF_3, which also supports the aforementioned contention of stronger interaction of CO_2 in MeMOFs than in

FMOFs. The same analogy could also be made for CH_4 interaction, as suggested upon comparing the distances between H_CH_4 – F_CF_3 vs H_CH_4 – H_CH_3 even after considering the covalent radius difference between F vs H.

Given that the DFT calculations suggest that the interaction energy of CH_4 is stronger with the -CH_3 group in MeMOF-1 compared to the -CF_3 group in FMOF-1c, one may ascribe that to stronger interactions of CH_4 molecules with the -CF_3 groups due to the presence of a partial negative charge on the rather electronegative F atoms. In contrast, the H atoms on the -CH_3 group possess partial positive charges, and one might expect repulsive forces among H atoms of CH_4 molecule and the -CH_3 group. However, the calculations suggest an attractive C-H···H-C interaction (even higher than C-F···H-C interaction), which is not surprising. This could be explained by the dispersion stabilization of CH_4 molecules based on the valence bond (VB) model, as studied by Danovich et al.[85] The VB analysis revealed that the stabilization of C^{+}-H^{-}···H^{+}-C^{-} interaction arises due to the alternation of atomic charges (i.e., $C^{-}H^{+}\cdots H^{-}C^{+}$ and C-H···H-C), hence bringing about an electrostatic interaction. This phenomenon is consistent with the classical mechanism of oscillating dipoles as the source of dispersion interactions. The existence of attractive C-H···H-C interaction was further confirmed by other researchers based on theoretical calculations, using "Quantum Theory of Atoms in Molecules" (QTAIM) in planer aromatic system.[86–90]

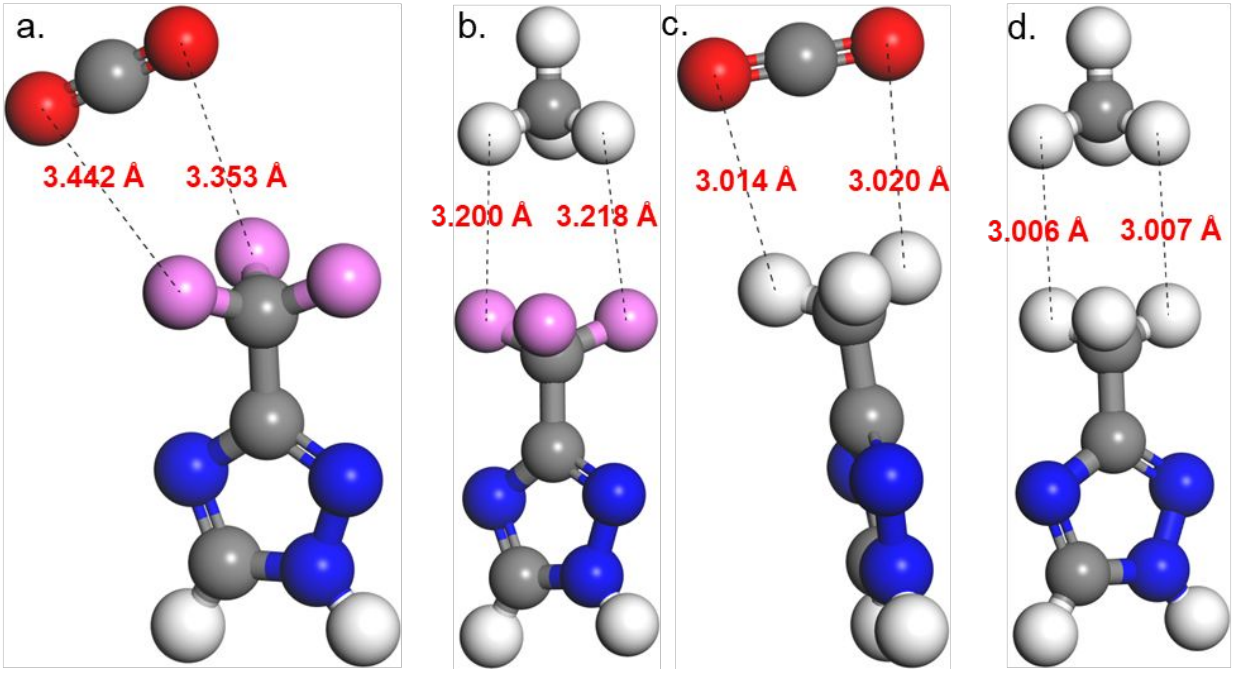

Figure 10. DFT-optimized structures of the parent CF_3-substituted linker with (a) CO_2 and (b) CH_4; and methyl-functionalized linker with (c) CO_2 and (d) CH_4. Color code (O: red, F: pink, N: blue, C: gray, and H: white).

3.6 Selectivity and Hydrophobicity of the MOFs

We have investigated the MeMOFs vs FMOFs for their selective adsorption of CO_2 or CH_4 over water. As shown in Figure S74, the CO_2 and CH_4 adsorption selectivity values over H_2O were comparable, obtained by two different methods (discussed in Section 2.3; vide supra) for FMOF-1c at 298 K. The selectivity of CO_2 over water in FMOF-1c is 6.4, derived from GCMC, whereas the value is 6.5 acquired from Henry's constant ratio. The selectivity of CH_4 over water in FMOF-1c is 4.3 and 3.9 obtained from GCMC simulations and Henry's constant ratio, respectively. The CO_2/H_2O selectivity using GCMC simulations was examined from the binary mixture of CO_2 and water (CO_2: H_2O = 7: 2 at 80% RH, corresponding to 3280 Pa) at 0.15 bar and 298 K. For CH_4/H_2O selectivity, we modeled a binary mixture of CH_4 and water at 95% RH at 1 bar and 298 K.

The CO_2/H_2O and CH_4/H_2O selectivity for a set of MOFs were calculated by their Henry's constant ratios, as shown in Figure 11. We compared the results of different FMOF and MeMOF structures with those of a prototypical hydrophobic MOF, ZIF-8. The K_H values of CO_2, CH_4, and H_2O in ZIF-8 from our simulations are 2.01×10^{-5} mmol/g/Pa, 1.09×10^{-5} mmol/g/Pa and 2.61×10^{-6} mmol/g/Pa, respectively. These values are comparable to those obtained by Moghadam et al.[91] -- namely 1.50×10^{-5} mmol/g/Pa for CH_4 and 2.60×10^{-6} mmol/g/Pa for H_2O -- suggesting a good validation for our methodology. Overall, the results suggest that ZIF-8 has the largest K_H values for "dry" CO_2 and CH_4, as expected for such a high-surface-area standard hydrophobic framework.

The highest selectivity of CO_2 over H_2O was obtained for MeMOF-1c with a value of 11.9. ZIF-8 shows the largest K_H for H_2O among all the hydrophobic structures investigated. The higher CO_2/H_2O selectivity of MeMOF-1c compared to ZIF-8 is due to the relatively lower K_H value of H_2O adsorption in MeMOF-1c vs that in ZIF-8. On the other hand, FMOF-1a shows the highest selectivity of CH_4 over H_2O -- likely due to its lowest H_2O K_H value. The CH_4/H_2O selectivity was 5.7 for FMOF-1a, which is higher compared to ZIF-8, whereas all other structures showed similar lower values comparatively.

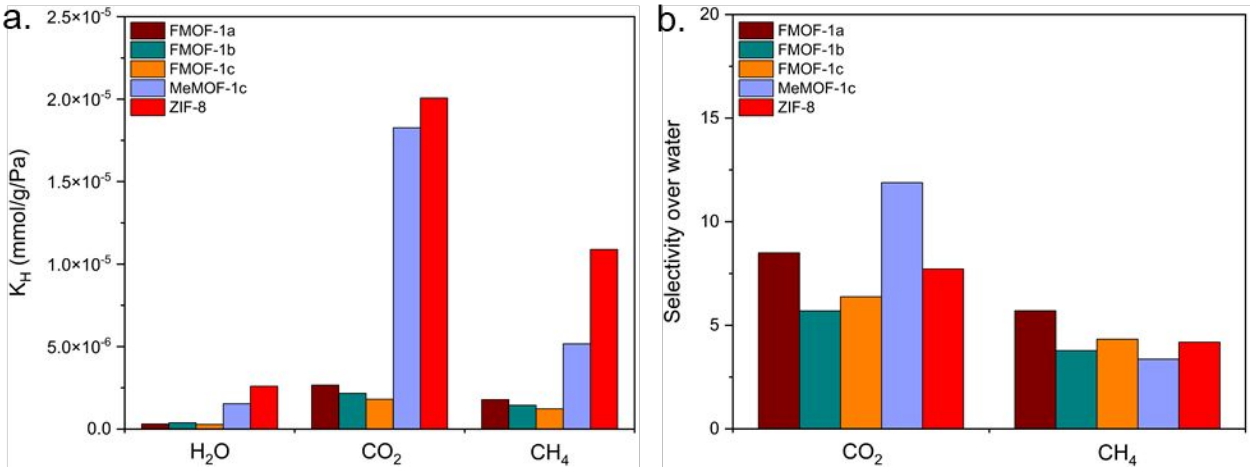

Figure 11. (a) Henry's constant (K_H) for H_2O, CO_2, and CH_4 at 298 K; (b) adsorption selectivity of CO_2 and CH_4 over water for various MOFs at 298 K.

The simulated pure component water adsorption isotherms are presented in Figure 12 for both the parent -CF_3 and the -CH_3 functionalized MOFs at 298 K. As water interaction is highly sensitive to the charges of framework atoms, we have used two different charge methods, CBAC[56] and EQeq,[71] to predict the water adsorption isotherm of the adsorbents. Type V water adsorption profile was observed for MeMOF-1c, indicating the presence of weak interactions between the adsorbate and the adsorbent, using the CBAC method. The water condensation pressure, P_c, for MeMOF-1c was found to be 4500 Pa, close to saturation. In contrast, these simulations do not predict any water condensation in MeMOF-1c based on the EQeq method. Likewise, no water condensation pressure was found for FMOF-1c. Figure S75 shows the number of water molecules adsorbed in FMOF-1c at 298 K and at 4500 Pa as a function of number of MC cycles. This graph confirms the water convergence in hydrophobic FMOF structures, and thus we determine that water adsorption isotherms showed in Figure 12 are reliable.

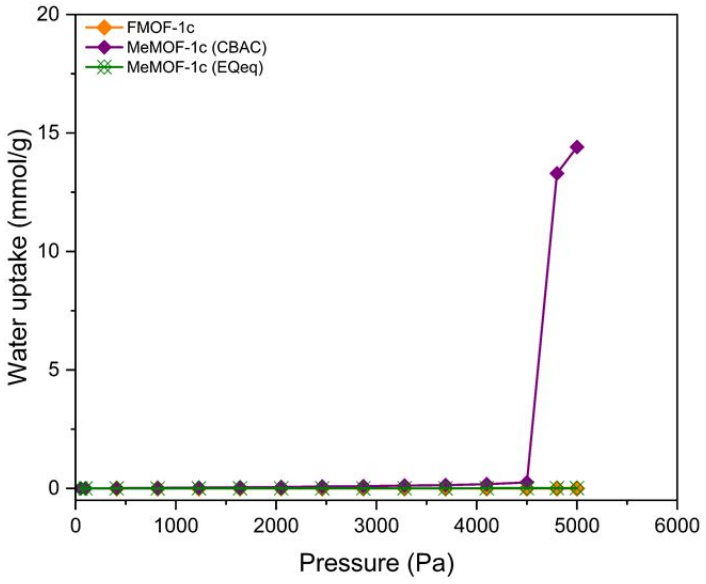

Figure 12. Water uptake for FMOF-1c and MeMOF-1c at 298 K.

Lastly, we have used GCMC simulation to model a binary mixture of CH_4 and water at 80% relative humidity to examine the influence of water/high humidity on CH_4 uptake in FMOF-

1c (Figure 13) and MeMOF-1c (Figure 14). The isotherms show similar CH_4 uptake, under both dry and wet conditions, demonstrating negligible loss of CH_4 uptake at 80% relative humidity in FMOF-1c. The impact of humidity on CO_2 and CH_4 adsorption in MeMOF-1c was also considered to study the result of -CH_3 functionalization on CO_2 and CH_4 uptake under humid condition (Figure 14). Thus, GCMC simulations were performed to obtain excess adsorption isotherms for pure-component CO_2 and CH_4 as well as binary mixtures of CO_2/H_2O and CH_4/H_2O at 80% RH at 298 K in MeMOF-1c (Figure 14). MeMOF-1c exhibits a much higher uptake of CO_2 and CH_4 than H_2O. Although the interaction of H_2O with the methyl-functionalized MOF, MeMOF-1c, is higher than that of the parent MOF, FMOF-1c, this higher H_2O interaction did not affect the CO_2 and CH_4 uptake significantly in MeMOF-1c at 80% RH (Figure 14). We speculate this nominal influence on CO_2 and CH_4 uptake in MeMOF-1c is due to the lower partial pressure of water (3280 Pa) than the observed water condensation pressure (4500 Pa). We simulated the 80% RH by fixing the partial pressure of water at 3280 Pa through the entire isotherm, based on the vapor pressure (4100 Pa) predicted by the *TIP4P* water model. As shown in Figure 12, water condensation occurs at 4500 Pa, which is higher than the partial pressure of water (3280 Pa) in the binary mixture.

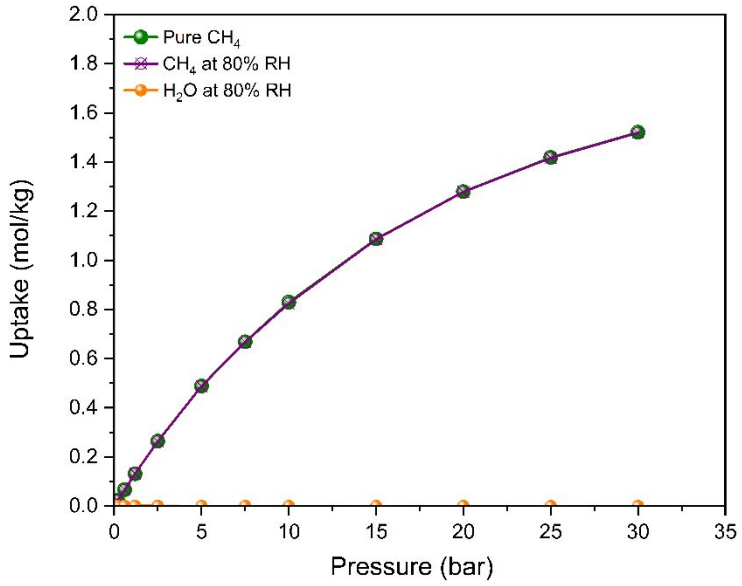

Figure 13. Adsorption isotherms of pure component CH_4 and a binary mixture of CH_4 and H_2O at 80% relative humidity in FMOF-1c at 298 K.

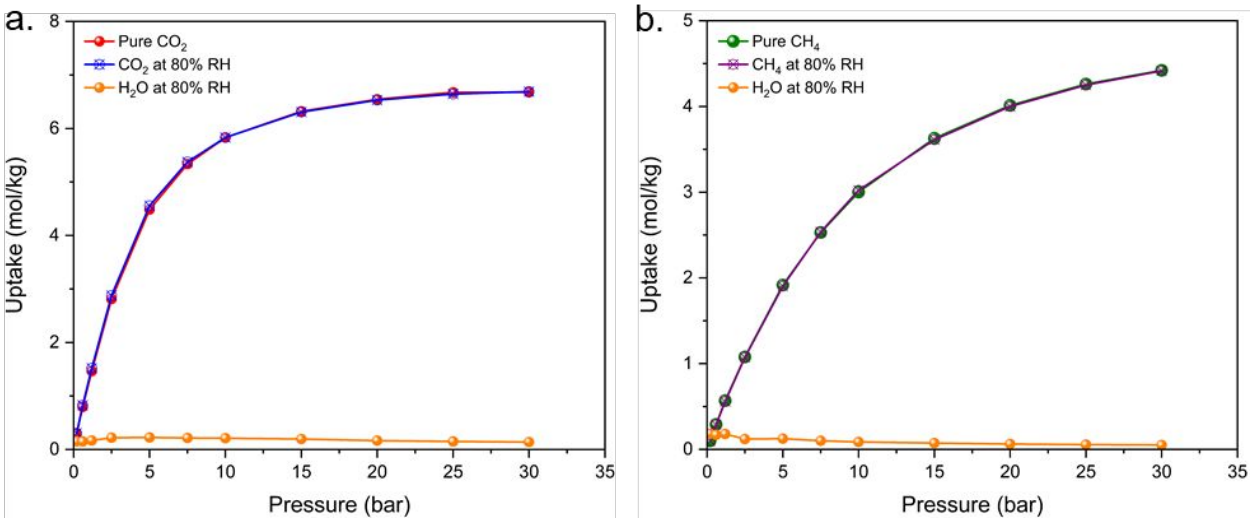

Figure 14. Adsorption isotherms of (a) pure component CO_2 and a binary mixture of CO_2 and H_2O at 80% relative humidity and (b) pure component CH_4 and a binary mixture of CH_4 and water at 80% relative humidity in MeMOF-1c at 298 K.

3.7 Experimental Validation of PXRD Pattern and Superhydrophobicity of MeMOFs

The successful synthesis of a MeMOF-2 composition, corresponding to the same {Ag(3,5-$(CH_3)_2$-1,2,4-triazolate)} empirical formula of the simulated structures, was confirmed by powder

X-ray diffraction (PXRD). The PXRD pattern for this synthesized material, however, corresponded to that of a different crystal structure pattern published by Zhai et al.[67] The two patterns show excellent agreement, as shown in Figure 15a.

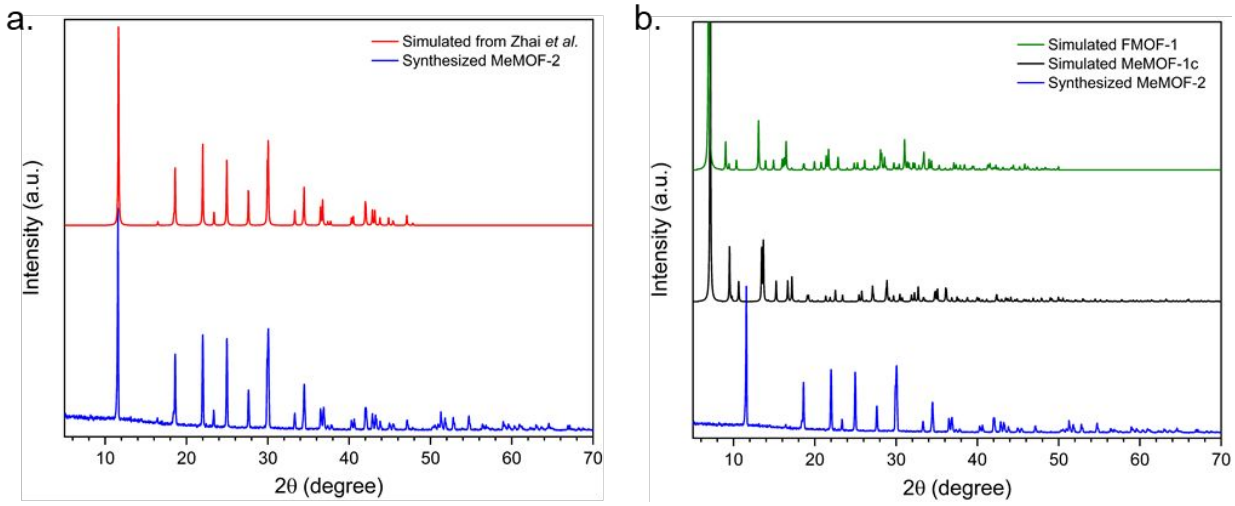

Figure 15. (a) PXRD pattern of the synthesized MeMOF-2 herein (blue) overlaid with the published PXRD pattern by Zhai et al. (red) [67] and (b) experimental PXRD pattern of the experimentally-prepared MeMOF-2 sample herein (blue) overlaid with the simulated PXRD patterns corresponding to the experimental crystal structure of FMOF-1[45] (green) and the hypothetical MeMOF-1c analogue thereof (black).

It should be noted that the structure from the simulated MeMOF-1 and the synthesized MeMOF-2 are dissimilar, as revealed by the PXRD pattern in Figure 15b, but more similar to the analogous FMOF-1 structure even after the $CF_3 \rightarrow CH_3$ replacement. This underscores the complexity of prediction to synthesis. Despite this, the retention of the predicted hydrophobic property in the synthesized compound, based on contact angle measurements (Figure 16), suggests that the underlying design principles is still valuable. A crystal structure or PXRD pattern with the same $Ag_2[Ag_4Tz_6]$ unit cell formula and topology as those simulated hypothetical structures for MeMOF-1a/1b/1c that correspond to the analogous FMOF-1a/1b/1c experimental structures have not yet been isolated. Also, GCMC simulations of $CH_4/CO_2/H_2O$ adsorption for the experimental

structure of MeMOF-2 that we have synthesized, which corresponds to that reported by Zhai et al.[67] are not feasible because of the very low porosity of this experimental structure compared to MeMOF-1a/1b/1c hypothetical structures. Nevertheless, the simulations for the hypothetical structures are still valuable not only in anticipation of culmination of our ongoing efforts to isolate those or other porous structures experimentally but also for the experimental and other possible low-porosity MeMOF-2 compositions corresponding to the same {Ag(3,5-$(CH_3)_2$-1,2,4-triazolate)} empirical formula. This is because the guest adsorption and water repulsion attributes are generally a function of the surface interaction energy of a given guest molecule with the surface functional group of the MOF, which is little-dependent on porosity. This is validated by the general agreement of the DFT simulations for CH_4/CO_2 with the 3,5-$(CH_3)_2$-1,2,4-TzH ligand in Table 4 with the GCMC-derived Qst$_0$ values in Tables 2-3 (and analogous comparisons for FMOF-1[37] further validated by experimental Qst values). Furthermore, Galli et al.[39] have reported that another water repulsion metric, low-κ (dielectric constant) at high humidity, was sustained and even slightly enhanced for FMOF-1 samples when pressed at very high pressure that rendered them amorphous instead of crystalline (hence greatly reducing their porosity).

We have sought experimental validation of the GCMC-predicted hydrophobicity of the MeMOF-2 composition, $[Ag(Me_2Tz)]_\infty$. As shown in Figure 16, the PET plastic substrate exhibits an increase in water-drop contact angle by an ~100°, from ~74° (mere hydrophobic) to ~172° (superhydrophobic) range. This contact angle for MeMOF-2@PET is similar to, indeed slightly higher than, that (~160°) we had reported for a neat pellet of FMOF-1 formed spontaneously after the high-pressure CO_2 adsorption experiment[37] and significantly higher than the FMOF-1@PET sample (~131°) tested herein at the same conditions for comparison.

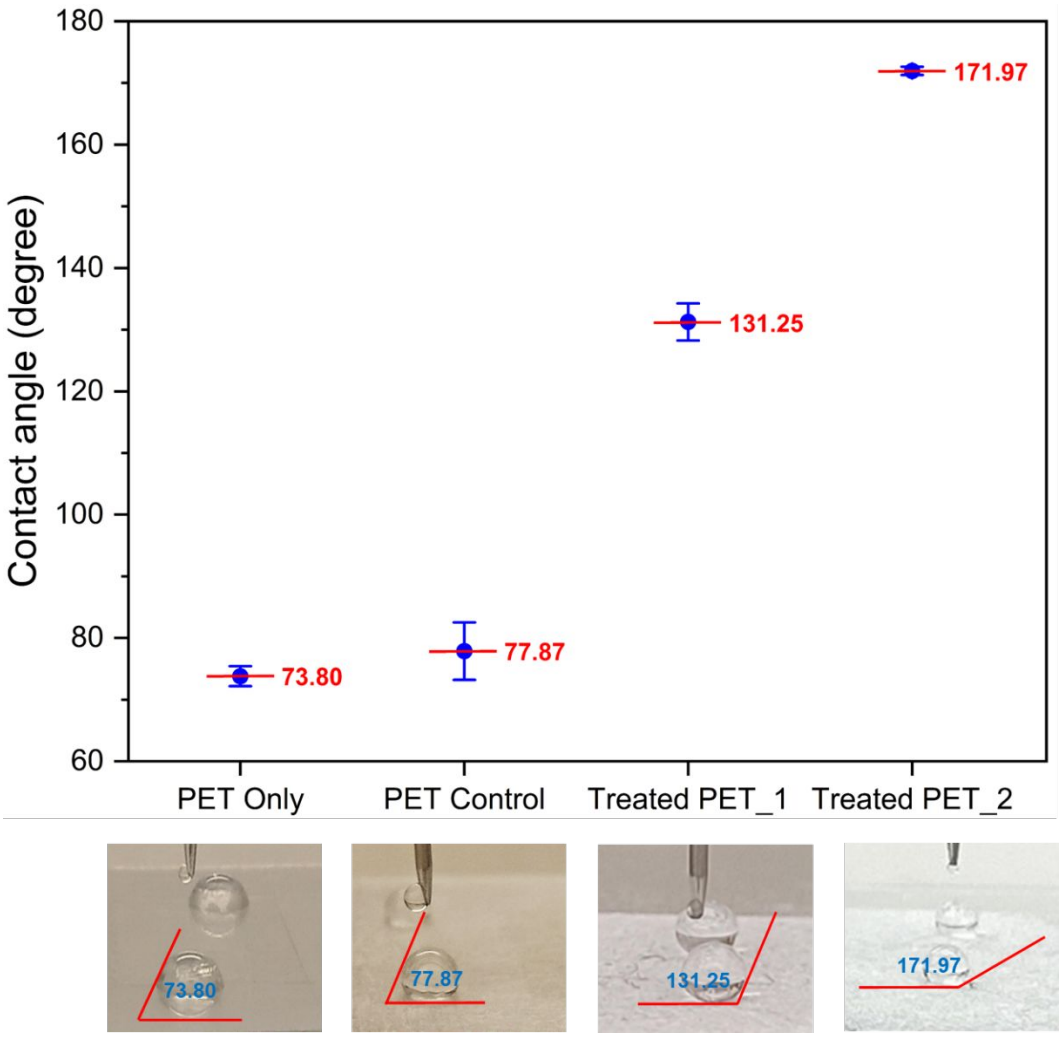

Figure 16. Water-drop contact angle data for PET only, PET control (sanded), treated PET_1 (FMOF-1@PET), and treated PET_2 (MeMOF-2@PET) from left-to-right, respectively. Contact angle values are shown as average ± standard deviation for triplicate (n = 3) measurements.

4. CONCLUSIONS

GCMC simulations were performed to study the CO_2 and CH_4 adsorption isotherms at three different temperatures (288, 298, and 308 K) in parent, FMOF-1, and analogous methyl-functionalized, MeMOF-1, structures, whereby CF_3 groups in FMOF-1 were replaced by CH_3, using a force field that has been validated. The thermodynamic parameters (Henry's constants and isosteric heat of adsorption at infinite dilution) were obtained directly from MC simulations

(rWidom insertion method). The adsorption isotherms generated by molecular simulations were fitted to the Langmuir, Freundlich-Langmuir and Tóth models. The Tóth model showed the best fit for both CO_2 and CH_4 in FMOF-1 and MeMOF-1 at the three aforementioned temperatures indicated by the lower residual root mean square error and chi-square values. Our results of Henry's constants (K_H) and isosteric heat of adsorption at infinite dilution (Q_{st0}), either obtained during the simulation or by using the Tóth isotherm model are very consistent and demonstrate that CO_2 and CH_4 have greater affinity to MeMOF-1 than FMOF-1 and for the same MOF the order is $CO_2 > CH_4$ indicated by the higher K_H and Q_{st0}. The larger uptake of CO_2 and CH_4 in MeMOF-1 predicted by GCMC simulations was found to be due to the effect of $-CH_3$ functionalization of FMOF-1. The selectivity and hydrophobicity were also investigated. The findings exhibited that water either does not condense at all, in one model, or condenses near saturation at 4500 Pa, in another model, in MeMOF-1, similar to the FMOF-1c behavior that exhibited no water condensation in either model. Most importantly, no loss of CO_2 and CH_4 uptake are found at 80% RH in the methyl-functionalized MOFs. Hence, MeMOF-1 is a promising candidate for CO_2 and CH_4 capture under humid conditions, suggesting that MeMOFs are potential fluorine-free superhydrophobic alternatives to FMOF, ZIF, Teflon, and PFAS materials. Finally, proof-of-concept experimental data have validated the superhydrophobic nature of the MeMOF-2 composition, which increased the water-drop contact angle from ~74° to ~172° upon dry-coating a plastic substrate with MeMOF-2.

ASSOCIATED CONTENT

Supplementary Information

The Electronic Supplementary Information (ESI) is available free of cost at .....

Optimized geometry of -CH_3 functionalized MOFs; interaction parameters; adsorption isotherm fitting details; isosteric heats of adsorption; Henry's constant; adsorption selectivity (PDF)

AUTHOR INFORMATION

Corresponding Authors

Mohammad A. Omary - *Department of Chemistry, University of North Texas, 1155 Union Circle, Denton, Texas-76203, United States;*
ORCID: 0000-0002-3247-3449;
Email: Omary@unt.edu

Jincheng Du - *Department of Materials Science and Engineering, University of North Texas, 1155 Union Circle, Denton, Texas-76203, United States;*
ORCID: 0000-0003-4805-7498;
Email: Jincheng.Du@unt.edu

Other Contributing Authors

Rashida Yasmeen - *Department of Materials Science & Engineering, University of North Texas, 1155 Union Circle, Denton, Texas-76203, United States;*
ORCID: 0000-0003-1637-0615

Sheikh M. S. Islam - *Department of Chemistry, University of North Texas, 1155 Union Circle, Denton, Texas-76203, United States;*
ORCID: 0000-0001-6909-7865

Olajumoke M. Ayeni - *Department of Chemistry, University of North Texas, 1155 Union Circle, Denton, Texas-76203, United States;*
ORCID: 0009-0000-5460-8095

Peyman Z. Moghadam - *Department of Chemical Engineering, University College London, London WC1E 7JE, United Kingdom;*
ORCID: 0000-0002-1592-0139

DATA AVAILABILITY

The data supporting this article have been included as part of the Electronic Supplementary Information (ESI).

ACKNOWLEDGEMENTS

M.A.O. acknowledges support from the U.S. Nuclear Regulatory Commission (Award 31310023M0019), the U.S. Department of Defense (Award W911NF2210201), the Welch Foundation (B-1542), and the U.S. National Science Foundation (CHE-1413641 and an international supplement thereof, CHE-1545934). J.D. acknowledges support of his group's contribution from the U.S. National Science Foundation (CMMI-1662288) and in part by the Advanced Research Projects Agency-Energy (ARPA-E) of U.S. Department of Energy (DE AR0001613). The computational facilities have been supported by the National Science Foundation (CHE-1531468 and OAC-2117247) and the University of North Texas (Research Computing Services and Texas Advanced Computing Center).

REFERENCES

1 J. Liu, P. K. Thallapally, B. P. McGrail, D. R. Brown and J. Liu, *Chem. Soc. Rev.*, 2012, **41**, 2308–2322.

2 D. L. Royer, R. A. Berner and J. Park, *Nature*, 2007, **446**, 530–532.

3 Metz, B.; Davidson, O.; De Coninck, H. C.; Loos, M.; Meyer, L. *IPCC Special Report on Carbon Dioxide Capture and Storage*, Cambridge University Press, Cambridge, United Kingdom, 2005.

4 D. R. Feldman, W. D. Collins, P. J. Gero, M. S. Torn, E. J. Mlawer and T. R. Shippert, *Nature*, 2015, **519**, 339–343.

5 *Inventory of U.S. Greenhouse gas Emissions and Sinks: 1990-1994*, U. S. Environmental Protection Agency. Office of Policy, Planning and Evaluation: Washington, D.C., U.S.A, 1995.

6 L. Li, J. Yang, J. Li, Y. Chen and J. Li, *CrystEngComm*, 2013, **15**, 6782.

7 J. Park, H. Cha, S. Song and K. M. Chun, *Int J Hydrogen Energy*, 2011, **36**, 5153–5162.

8 K. Sumida, D. L. Rogow, J. A. Mason, T. M. McDonald, E. D. Bloch, Z. R. Herm, T.-H. Bae and J. R. Long, *Chem Rev*, 2012, **112**, 724–781.

9 J. Yu, S. Wang and H. Yu, *International Journal of Greenhouse Gas Control*, 2016, **50**, 135–146.

10 G. T. Rochelle, *Science (1979)*, 2009, **325**, 1652–1654.

11 Y. Lin, *Curr Opin Chem Eng*, 2015, **8**, 21–28.

12 J. Y. S. Lin, *Science (1979)*, 2016, **353**, 121–122.

13 Y. Wu, X. Chen, M. Fan, G. Jiang, Y. Kong and A. E. Bland, *Chemical Engineering Journal*, 2015, **262**, 1192–1198.

14 Q. Yang, C. Zhong and J.-F. Chen, *The Journal of Physical Chemistry C*, 2008, **112**, 1562–1569.

15 S. Yang, Z. Liu, X. Yan, C. Liu, Z. Zhang, H. Liu and L. Chai, *Energy & Fuels*, 2019, **33**, 11380–11388.

16 J. Hu, Y. Liu, J. Liu and C. Gu, *AIChE Journal*, DOI:10.1002/aic.16835.

17 D. M. D'Alessandro, B. Smit and J. R. Long, *Angewandte Chemie International Edition*, 2010, **49**, 6058–6082.

18 G. Férey, *Chem. Soc. Rev.*, 2008, **37**, 191–214.

19 J. R. Long and O. M. Yaghi, *Chem Soc Rev*, 2009, **38**, 1213.

20 A. Pal, S. Chand and M. C. Das, *Inorg Chem*, 2017, **56**, 13991–13997.

21 J. L. C. Rowsell and O. M. Yaghi, *J Am Chem Soc*, 2006, **128**, 1304–1315.

22 Y. F. Chen, A. Nalaparaju, M. Eddaoudi and J. W. Jiang, *Langmuir*, 2012, **28**, 3903–3910.

23 S. Li, Y. G. Chung, C. M. Simon and R. Q. Snurr, *J Phys Chem Lett*, 2017, **8**, 6135–6141.

24 J. An and N. L. Rosi, *J Am Chem Soc*, 2010, **132**, 5578–5579.

25 X.-J. Wang, P.-Z. Li, Y. Chen, Q. Zhang, H. Zhang, X. X. Chan, R. Ganguly, Y. Li, J. Jiang and Y. Zhao, *Sci Rep*, 2013, **3**, 1149.

26 X. Liu, M. Park, S. Hong, M. Oh, J. W. Yoon, J.-S. Chang and M. S. Lah, *Inorg Chem*, 2009, **48**, 11507–11509.

27 K. K. Tanabe and S. M. Cohen, *Chem. Soc. Rev.*, 2011, **40**, 498–519.

28 J. Hu, Y. Liu, J. Liu and C. Gu, *Fuel*, 2017, **200**, 244–251.

29 Z. Xiang, S. Leng and D. Cao, *The Journal of Physical Chemistry C*, 2012, **116**, 10573–10579.

30 B. Zheng, J. Bai, J. Duan, L. Wojtas and M. J. Zaworotko, *J Am Chem Soc*, 2011, **133**, 748–751.

31 J. An, S. J. Geib and N. L. Rosi, *J Am Chem Soc*, 2010, **132**, 38–39.

32 Y. Ye, H. Zhang, L. Chen, S. Chen, Q. Lin, F. Wei, Z. Zhang and S. Xiang, *Inorg Chem*, 2019, **58**, 7754–7759.

33 J. Liu, A. I. Benin, A. M. B. Furtado, P. Jakubczak, R. R. Willis and M. D. LeVan, *Langmuir*, 2011, **27**, 11451–11456.

34 A. C. Kizzie, A. G. Wong-Foy and A. J. Matzger, *Langmuir*, 2011, **27**, 6368–6373.

35 S. Keskin, T. M. van Heest and D. S. Sholl, *ChemSusChem*, 2010, **3**, 879–891.

36 H. Furukawa, F. Gándara, Y.-B. Zhang, J. Jiang, W. L. Queen, M. R. Hudson and O. M. Yaghi, *J Am Chem Soc*, 2014, **136**, 4369–4381.

37 P. Z. Moghadam, J. F. Ivy, R. K. Arvapally, A. M. dos Santos, J. C. Pearson, L. Zhang, E. Tylianakis, P. Ghosh, I. W. H. Oswald, U. Kaipa, X. Wang, A. K. Wilson, R. Q. Snurr and M. A. Omary, *Chem Sci*, 2017, **8**, 3989–4000.

38 C. Yang, U. Kaipa, Q. Z. Mather, X. Wang, V. Nesterov, A. F. Venero and M. A. Omary, *J Am Chem Soc*, 2011, **133**, 18094–18097.

39 S. Galli, A. Cimino, J. F. Ivy, C. Giacobbe, R. K. Arvapally, R. Vismara, S. Checchia, M. A. Rawshdeh, C. T. Cardenas, W. K. Yaseen, A. Maspero and M. A. Omary, *Adv Funct Mater*, DOI:10.1002/adfm.201904707.

40 T.-H. Chen, I. Popov, O. Zenasni, O. Daugulis and O. Š. Miljanić, *Chemical Communications*, 2013, **49**, 6846.

41 Z. Zhang and O. Š. Miljanić, *Organic Materials*, 2019, **01**, 019–029.

42 Z. Zhang, T. Lieu, C.-H. Wu, X. Wang, J. I. Wu, O. Daugulis and O. Š. Miljanić, *Chemical Communications*, 2019, **55**, 9387–9390.

43 Z. Yang, S. Wang, Z. Zhang, W. Guo, K. Jie, M. I. Hashim, O. Š. Miljanić, D. Jiang, I. Popovs and S. Dai, *J Mater Chem A Mater*, 2019, **7**, 17277–17282.

44 T.-H. Chen, I. Popov, W. Kaveevivitchai, Y.-C. Chuang, Y.-S. Chen, O. Daugulis, A. J. Jacobson and O. Š. Miljanić, *Nat Commun*, 2014, **5**, 5131.

45 C. Yang, X. Wang and M. A. Omary, *J Am Chem Soc*, 2007, **129**, 15454–15455.

46 Accelrys Software Inc., Material Studio Modeling Environment, Release 6, Accelrys Software Inc., San Diego, California, USA, 2011.

47 A. K. Rappe, C. J. Casewit, K. S. Colwell, W. A. Goddard and W. M. Skiff, *J Am Chem Soc*, 1992, **114**, 10024–10035.

48 D. A. Gomez-Gualdron, O. V. Gutov, V. Krungleviciute, B. Borah, J. E. Mondloch, J. T. Hupp, T. Yildirim, O. K. Farha and R. Q. Snurr, *Chemistry of Materials*, 2014, **26**, 5632–5639.

49 O. K. Farha, A. Özgür Yazaydın, I. Eryazici, C. D. Malliakas, B. G. Hauser, M. G. Kanatzidis, S. T. Nguyen, R. Q. Snurr and J. T. Hupp, *Nat Chem*, 2010, **2**, 944–948.

50 O. V. Gutov, W. Bury, D. A. Gomez-Gualdron, V. Krungleviciute, D. Fairen-Jimenez, J. E. Mondloch, A. A. Sarjeant, S. S. Al-Juaid, R. Q. Snurr, J. T. Hupp, T. Yildirim and O. K. Farha, *Chemistry – A European Journal*, 2014, **20**, 12389–12393.

51 T. Düren, Y.-S. Bae and R. Q. Snurr, *Chem Soc Rev*, 2009, **38**, 1237.

52 J. G. McDaniel, S. Li, E. Tylianakis, R. Q. Snurr and J. R. Schmidt, *The Journal of Physical Chemistry C*, 2015, **119**, 3143–3152.

53 Frenkel, D.; Smit, B. *Understanding Molecular Simulation: From Algorithm to Applications*; Elsevier Inc.: Third Edition, 2023.

54 P. P. Ewald, *Ann Phys*, 1921, **369**, 253–287. https://doi.org/10.1002/andp.19213690304.

55 V. H. Dalvi, V. Srinivasan and P. J. Rossky, *The Journal of Physical Chemistry C*, 2010, **114**, 15553–15561.

56 Q. Xu and C. Zhong, *The Journal of Physical Chemistry C*, 2010, **114**, 5035–5042.

57 J. J. Potoff and J. I. Siepmann, *AIChE Journal*, 2001, **47**, 1676–1682.

58 A. M. Fracaroli, H. Furukawa, M. Suzuki, M. Dodd, S. Okajima, F. Gándara, J. A. Reimer and O. M. Yaghi, *J Am Chem Soc*, 2014, **136**, 8863–8866.

59 W. L. Jorgensen, J. Chandrasekhar, J. D. Madura, R. W. Impey and M. L. Klein, *J Chem Phys*, 1983, **79**, 926–935.

60 D. Dubbeldam, S. Calero, D. E. Ellis and R. Q. Snurr, *Mol Simul*, 2016, **42**, 81–101.

61 D.-Y. Peng and D. B. Robinson, *Industrial & Engineering Chemistry Fundamentals*, 1976, **15**, 59–64.

62 B. Widom, *J Chem Phys*, 1963, **39**, 2808–2812.

63 S. Grimme, S. Ehrlich and L. Goerigk, *J Comput Chem*, 2011, **32**, 1456–1465.

64 J. Baker, *J Comput Chem*, 1986, **7**, 385–395.

65 T. F. Willems, C. H. Rycroft, M. Kazi, J. C. Meza and M. Haranczyk, *Microporous and Mesoporous Materials*, 2012, **149**, 134–141.

66 Gaussian 16, Revision C.01, M. J. Frisch, G. W. Trucks, H. B. Schlegel, G. E. Scuseria, M. A. Robb, J. R. Cheeseman, G. Scalmani, V. Barone, G. A. Petersson, H. Nakatsuji, X. Li, M. Caricato, A. V. Marenich, J. Bloino, B. G. Janesko, R. Gomperts, B. Mennucci, H. P. Hratchian, J. V. Ortiz, A. F. Izmaylov, J. L. Sonnenberg, D. Williams-Young, F. Ding, F. Lipparini, F. Egidi, J. Goings, B. Peng, A. Petrone, T. Henderson, D. Ranasinghe, V. G. Zakrzewski, J. Gao, N. Rega, G. Zheng, W. Liang, M. Hada, M. Ehara, K. Toyota, R. Fukuda, J. Hasegawa, M. Ishida, T. Nakajima, Y. Honda, O. Kitao, H. Nakai, T. Vreven, K. Throssell, J. A. Montgomery, Jr., J. E. Peralta, F. Ogliaro, M. J. Bearpark, J. J. Heyd, E. N. Brothers, K. N. Kudin, V. N. Staroverov, T. A. Keith, R. Kobayashi, J. Normand, K. Raghavachari, A. P. Rendell, J. C. Burant, S. S. Iyengar, J. Tomasi, M. Cossi, J. M. Millam, M. Klene, C. Adamo, R. Cammi, J. W. Ochterski, R. L. Martin, K. Morokuma, O. Farkas, J. B. Foresman, and D. J. Fox, Gaussian, Inc., Wallingford CT, 2016.67 Q.-G. Zhai, M.-C. Hu, S.-N. Li and Y.-C. Jiang, *Inorganica Chim Acta*, 2009, **362**, 1355–1357.

67 Q.-G. Zhai, M.-C. Hu, S.-N. Li and Y.-C. Jiang, *Inorganica Chim Acta*, 2009, **362**, 1355–1357.

68 W. Chen, W. Wang, D. X. Luong, J. T. Li, V. Granja, P. A. Advincula, C. Ge, Y. Chyan, K. Yang, W. A. Algozeeb, C. F. Higgs and J. M. Tour, *ACS Appl Mater Interfaces*, 2022, **14**, 35053–35063.

69 R. Babarao and J. Jiang, *Langmuir*, 2008, **24**, 6270–6278.

70 N. Nijem, P. Canepa, U. Kaipa, K. Tan, K. Roodenko, S. Tekarli, J. Halbert, I. W. H. Oswald, R. K. Arvapally, C. Yang, T. Thonhauser, M. A. Omary and Y. J. Chabal, *J Am Chem Soc*, 2013, **135**, 12615–12626.

71 C. E. Wilmer, K. C. Kim and R. Q. Snurr, *J Phys Chem Lett*, 2012, **3**, 2506–2511.

72 S. M. S. Islam, R. Yasmeen, G. Verma, S. M. Tekarli, V. N. Nesterov, S. Ma and M. A. Omary, *Inorg Chem*, 2024, **63**, 8664–8673.

73 H. W. B. Teo, A. Chakraborty and S. Kayal, *Appl Therm Eng*, 2017, **110**, 891–900.

74 R. Yasmeen, S. M. S. Islam, J. Du and M. Omary, *Dalton Transactions*, 2025. DOI:10.1039/D4DT03093A.

75 K. A. Forrest, T. Pham, A. Hogan, K. McLaughlin, B. Tudor, P. Nugent, S. D. Burd, A. Mullen, C. R. Cioce, L. Wojtas, M. J. Zaworotko and B. Space, *The Journal of Physical Chemistry C*, 2013, **117**, 17687–17698.

76 J. A. Mason, M. Veenstra and J. R. Long, *Chem. Sci.*, 2014, **5**, 32–51.

77 G. Xiong, B.-B. Wang, L.-X. You, B.-Y. Ren, Y.-K. He, F. Ding, I. Dragutan, V. Dragutan and Y.-G. Sun, *J Mater Chem A Mater*, 2019, **7**, 393–404.

78 C. E. Wilmer, O. K. Farha, Y.-S. Bae, J. T. Hupp and R. Q. Snurr, *Energy Environ Sci*, 2012, **5**, 9849.

79 T. Pham, K. A. Forrest, E. H. L. Falcão, J. Eckert and B. Space, *Physical Chemistry Chemical Physics*, 2016, **18**, 1786–1796.

80 L. Qu, Z. Wang and L. Liu, *Fire*, 2023, **6**, 355.

81 *The periodic table of the elements*. WebElements. https://webelements.com/ (accessed Feb 17, 2025).

82 H. Pan, J. A. Ritter and P. B. Balbuena, *Langmuir*, 1998, **14**, 6323–6327.

83 C. Gu, Y. Liu, W. Wang, J. Liu and J. Hu, *Front Chem Sci Eng*, 2021, **15**, 437–449.

84 R. Paulini, K. Müller and F. Diederich, *Angewandte Chemie International Edition*, 2005, **44**, 1788–1805.

85 D. Danovich, S. Shaik, F. Neese, J. Echeverría, G. Aullón and S. Alvarez, *J Chem Theory Comput*, 2013, **9**, 1977–1991.

86 R. F. W. Bader, *Atoms in Molecules: A Quantum Theory*. Oxford University Press: Walton Street, Oxford, United Kingdom, 1990.

87 C. F. Matta, J. Hernández-Trujillo, T. Tang and R. F. W. Bader, *Chemistry – A European Journal*, 2003, **9**, 1940–1951.

88 J. Hernández-Trujillo and C. F. Matta, *Struct Chem*, 2007, **18**, 849–857.

89 L. F. Pacios and L. Gómez, *Chem Phys Lett*, 2006, **432**, 414–420.

90 J. Echeverría, G. Aullón, D. Danovich, S. Shaik and S. Alvarez, *Nat Chem*, 2011, **3**, 323–330.

91 P. Z. Moghadam, D. Fairen-Jimenez and R. Q. Snurr, *J Mater Chem A Mater*, 2016, **4**, 529–536.

DATA AVAILABILITY

The data supporting this article have been included as part of the Electronic Supplementary Information (ESI).